Systematic approach to *B*-physics anomalies and *t*-channel dark matter

Giorgio Arcadi,[1,2,*] Lorenzo Calibbi[3,†] Marco Fedele[4,‡] and Federico Mescia[5,§]

[1]*Dipartimento di Matematica e Fisica, Università di Roma Tre and INFN Sezione di Roma Tre,
Via della Vasca Navale 84, 00146 Roma, Italy*
[2]*Dipartimento di Scienze Matematiche e Informatiche, Scienze Fisiche e Scienze della Terra,
Universita degli Studi di Messina, Via Ferdinando Stagno d'Alcontres 31, I-98166 Messina, Italy*
[3]*School of Physics, Nankai University, Tianjin 300071, China*
[4]*Institut für Theoretische Teilchenphysik, Karlsruhe Institute of Technology, D-76131 Karlsruhe, Germany*
[5]*Departamento de Física Quàntica i Astrofísica, Institut de Ciències del Cosmos (ICCUB),
Universitat de Barcelona, Martí i Franquès 1, E-08028 Barcelona, Spain*

We study renormalizable models with minimal field content that can provide a viable dark matter candidate through the standard freeze-out paradigm and, simultaneously, accommodate the observed anomalies in semileptonic *B*-meson decays at one loop. Following the hypothesis of minimality, this outcome can be achieved by extending the particle spectrum of the Standard Model either with one vectorlike fermion and two scalars or two vectorlike fermions and one scalar. The dark matter annihilations are mediated by *t*-channel exchange of other new particles contributing to the *B* anomalies, thus resulting in a correlation between flavor observables and dark matter abundance. Again based on minimality, we assume the new states to couple only with left-handed muons and second and third generation quarks. Besides an *ad hoc* symmetry needed to stabilize the dark matter, the interactions of the new states are dictated only by gauge invariance. We present here for the first time a systematic classification of the possible models of this kind, according to the quantum numbers of the new fields under the Standard Model gauge group. Within this general setup we identify a group of representative models that we systematically study, applying the most updated constraints from flavor observables, dedicated dark matter experiments, and LHC searches of leptons and/or jets and missing energy, and of disappearing charged tracks.

I. INTRODUCTION

The first decade of operation of the Large Hadron Collider (LHC) has resulted in the tremendous success represented by the discovery of the Higgs boson and provided us with a host of precise measurements and searches for new phenomena, finding no conclusive evidence of departures from the predictions of the Standard Model (SM). Nevertheless, the SM leaves unanswered a number of fundamental questions that provide strong motivation for its extension. The most compelling problem is that the SM lacks a candidate of dark matter (DM), whose existence has been established by an impressive number of

*giorgio.arcadi@unime.it
†calibbi@nankai.edu.cn
‡marco.fedele@kit.edu
§mescia@ub.edu

cosmological and astrophysical observations, spanning many orders of magnitude in redshift: from the cosmic microwave background (CMB) to galactic rotation curves, see Ref. [1] for a review. However, we do not have at the moment knowledge about the nature of dark matter nor about its mass and interactions with the SM sector, since all evidence is based on its gravitational effects. All direct and indirect searches for particle dark matter have so far given negative results. Nevertheless, it is plausible that DM interacts to some extent with the SM fields, as a substantial DM abundance must be produced in the early Universe. This is the case of the thermal freeze-out mechanism, which assumes that DM is a thermal relic, most commonly a weakly interacting massive particle (WIMP). Sizeable interactions to SM particles are then required to keep DM in thermal equilibrium with the SM bath in the early Universe and to ensure an efficient DM annihilation mechanism in order to avoid the WIMP relic density to be larger than the DM abundance that is observed today. In this work, we are going to assume that the observed DM density is accounted for by a thermal WIMP that interacts with SM quarks and leptons and other extra fields in a way that can address the so-called *B*-physics (or flavor) anomalies.
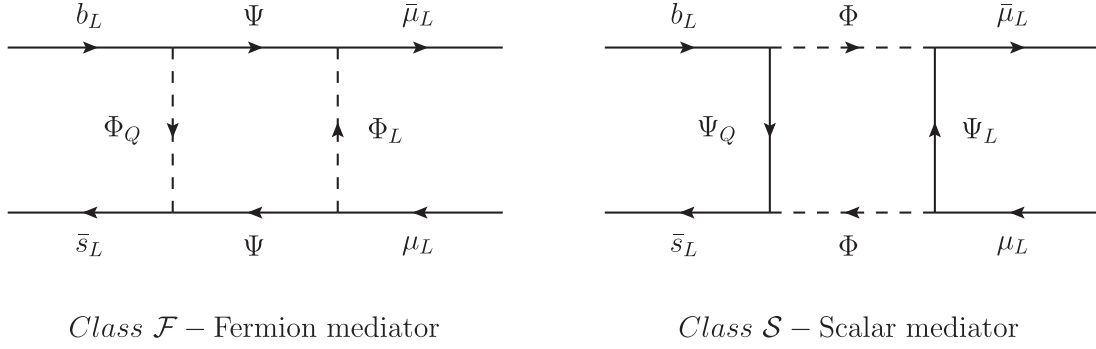
Class $\mathcal{F}$ − Fermion mediator   *Class* $\mathcal{S}$ − Scalar mediator

FIG. 1.   Basic diagrams contributing to $b \to s\mu\mu$.

In fact, although direct searches performed by the LHC Collaboration for the production of new particles have found no evidence of their existence, several experimental collaborations, with LHCb being the prominent one, have brought to light a persistent and coherent pattern of deviations from the SM predictions in semileptonic decays of B mesons of the kind $b \to s\ell^+\ell^-$. This could very well be the first experimental hint for beyond the SM (BSM) physics at energies not much larger than the electroweak scale. In particular, LHCb and B-factory experiments observe a deviation from lepton flavor universality (LFU) predicted by the SM in the theoretically clean observables $R_{K^{(*)}} \equiv \mathrm{BR}(B \to K^{(*)}\mu^+\mu^-)/\mathrm{BR}(B \to K^{(*)}e^+e^-)$ [2–4]. Moreover, a number of measurements are in tension with the SM predictions for the branching ratios and angular distributions of several $b \to s\mu^+\mu^-$ modes [5–14]. All these anomalies could be explained by a deficit of $b \to s\mu^+\mu^-$ events compared to SM expectations due to the interference between SM and BSM amplitudes. The simplest way to achieve such an effect is to add nonstandard contributions, $\delta C_\mu^{9,10}$, to the following operators:

$$\mathcal{H}_{\mathrm{eff}} \supset -\frac{4G_F}{\sqrt{2}}\frac{e^2}{16\pi^2} V_{tb}V_{ts}^*[C_\mu^9(\bar{s}\gamma_\mu P_L b)(\bar{\mu}\gamma^\mu\mu)$$
$$+ C_\mu^{10}(\bar{s}\gamma_\mu P_L b)(\bar{\mu}\gamma^\mu\gamma_5\mu) + \mathrm{H.c.}]. \quad (1)$$

While not providing the absolute best fit to the anomalies, an interesting scenario, still in excellent agreement with the data, is represented by $\delta C_\mu^9 = -\delta C_\mu^{10} \approx -0.5$, corresponding to the case of only left-handed currents entering Eq. (1). According to global fits to B-physics data, such a scenario is preferred to the SM prediction at the $\sim 5\sigma$ level [15–26]. This does not reflect, of course, an established breakdown of the SM: a combination of overlooked systematics, statistical fluctuations, and underestimated hadronic uncertainties could conspire to account for such a large deviation from the SM in the global fit. Nevertheless it is tempting to explore new physics (NP) scenarios that could explain the anomalies and assess their capability of addressing other shortcomings of the SM, in particular the DM problem.

In this paper we systematically build a set of simplified models that can explain the B-physics anomalies and simultaneously provide a good DM candidate, and we study their phenomenology with a particular focus on the LHC limits on production of new heavy particles and the bounds from direct- and indirect-detection DM searches. Our aim is to highlight the *minimal* building blocks that a more complete theory may need to include. For the sake of minimality we are going to employ the following procedure.

(i) We focus on minimal solutions of the B-physics anomalies of the $\delta C_\mu^9 = -\delta C_\mu^{10}$ kind; hence, we only introduce new fields—in the lowest possible number—that couple to left-handed quarks and leptons [the SM $SU(2)_L$ doublets].

(ii) We require that at least one of the BSM fields contains a state which can be a good DM candidate, i.e., a neutral and color singlet.

(iii) We assume that DM stability is ensured by an unbroken symmetry (a $\mathbf{Z}_2$ parity or another global symmetry), which forbids interactions between a NP particle and two SM particles, as well as mixing between NP and SM fields. As a consequence, the BSM contributions to C_μ^9 and C_μ^{10} can only arise through one-loop diagrams like those shown in Fig. 1 with only BSM fields running in the loop, as in the framework studied in Refs. [27–29]. Notice that for simplicity we only consider spin 0 and spin 1/2 fields and that only three new fields need to be added to the SM.

(iv) $SU(3)_c \otimes SU(2)_L \otimes U(1)_Y$ gauge invariance and the requirement of a consistent DM candidate tightly constrain the possible quantum numbers of the BSM fields. Furthermore, imposing the predicted relic density to be at (or below) the observed value $\Omega_{\mathrm{DM}}h^2 \simeq 0.12$ results in nontrivial conditions on the spectrum and couplings of the new particles, such that DM efficiently annihilates into SM particles. An unavoidable annihilation mode is given by the *t*-channel exchange of the other fields entering the loop of Fig. 1, possibly alongside coannihilations
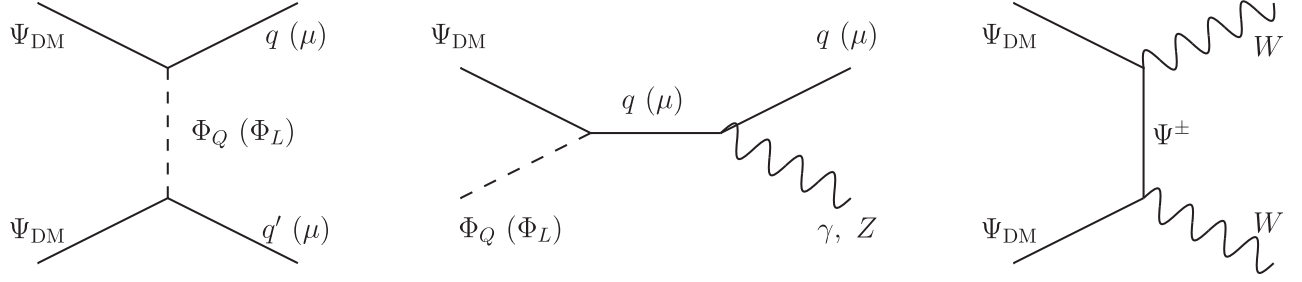
FIG. 2.   Illustrative DM (co-)annihilation diagrams for the case of fermion DM belonging to the field denoted as Ψ in Fig. 1. Analogous diagrams arise in the other cases. Gauge diagrams such as the third one are only present if DM belongs to an $SU(2)_L$ multiplet ($\Psi^\pm$ are charged states in the same multiplet).

and processes involving gauge interactions (if DM belongs to a nontrivial representation of the electroweak gauge group); see Fig. 2.

To the best of our knowledge, this is the first systematic study of the connection between flavor anomalies and dark matter. However, several previous works in the literature proposed specific models that fulfill the conditions outlined above, which then will be included in our classification; see Refs. [30–35]. Other works that addressed simultaneously DM and the *B*-physics anomalies (among other observables) include Refs. [36–58].

The outline of the paper is the following. In Sec. II we define our setup and show the set of minimal models that follows from the approach described above. In Sec. III we describe our strategy and how we impose constraints from *B* physics, LHC searches, and DM phenomenology. In Sec. IV we choose a number of representative models, for which the results of our analysis are presented in detail. Finally we summarize and conclude in Sec. V.

II. SETUP

As discussed above, we consider models that can give rise to the contributions to $b \to s\mu\mu$ processes shown in Fig. 1.[1] We classify our models in two classes according to the spin of the field that couples to both quarks and leptons—which we call "flavor mediator" independently of its quantum numbers—as follows.

Class $\mathcal{F}$. These models feature a vectorlike fermion Ψ as flavor mediator and two extra scalars Φ_Q and Φ_L coupling to the SM left-handed fermions with interactions described by the following Lagrangian:

$$\mathcal{L}_\mathcal{F} \supset \Gamma_i^Q \bar{Q}_i P_R \Psi \Phi_Q + \Gamma_i^L \bar{L}_i P_R \Psi \Phi_L + \text{H.c.} \quad (2)$$

Class $\mathcal{S}$. In these models, we introduce a scalar flavor mediator Φ and two fermions Ψ_Q and Ψ_L in vectorlike representations of the SM gauge group:

---

[1]If the mediator field is a real scalar singlet or a Majorana fermion singlet, additional crossed box diagrams must be taken into account; see [28,29].

$$\mathcal{L}_\mathcal{S} \supset \Gamma_i^Q \bar{Q}_i P_R \Psi_Q \Phi + \Gamma_i^L \bar{L}_i P_R \Psi_L \Phi + \text{H.c.} \quad (3)$$

In the spirit of our simplified-model approach, we are considering nonzero couplings of the new fields only to second and third generation left-handed quarks (Γ_2^Q, Γ_3^Q) and muons (Γ_2^L). For more definiteness we will use, throughout the paper, the following notation: $\Gamma_2^Q = \Gamma_s^Q$, $\Gamma_3^Q = \Gamma_b^Q$, and $\Gamma_2^L = \Gamma_\mu^L$. These couplings are defined in the basis where the down quark and charged-lepton mass matrices are flavor diagonal. Furthermore we assume a global symmetry, whose effect is to forbid mixing between extra fields and SM fields and ensure that the lightest new state is stable. This can be achieved by introducing an unbroken $\mathbf{Z}_2$ parity under which the SM fields are even and the new fields are odd or an equivalent continuous symmetry. Finally, unless otherwise stated, we will usually assume the interactions in the scalar potential—such as the unavoidable quartic couplings between our new scalars Φ_X and the Higgs field H of the form $\Phi_X^\dagger \Phi_X H^\dagger H$—are small enough to have only subdominant effects on the phenomenology of our models.

The possible gauge quantum numbers of the extra fields follow from the requirement of gauge invariance of the above Lagrangians and the additional condition that at least one component is uncolored and electrically neutral, so to provide a viable DM candidate. Considering that the involved SM fields only are quark doublets Q, whose quantum numbers under $SU(3)_c \otimes SU(2)_L \otimes U(1)_Y$ are $(\mathbf{3}, \mathbf{2}, 1/6)$, and lepton doublets L, $(\mathbf{1}, \mathbf{2}, -1/2)$, the new fields have to belong to the representations of $SU(3)_c$ and $SU(2)_L$ displayed in Table I. Notice that, while all the possible representations of $SU(3)_c$ are listed in Table I (as combinations involving larger representations would not feature any color singlet), in the case of $SU(2)_L$ only representations with dimension $d \leq 3$ are displayed. The hypercharge assignment is in general not unique but, as mentioned above, it is restricted by the requirement that at least one state is neutral, i.e., $Q = T_3 + Y = 0$. Setting the hypercharge of the flavor mediator (Ψ or Φ) as a free parameter X, the hypercharge of other fields are then

TABLE I. Possible gauge quantum numbers of the new fields appearing in the loop diagrams in Fig. 1. The displayed $SU(3)_c$ representations are all the ones possible that allow a DM candidate, while only $SU(2)_L$ representations with $d \leq 3$ are shown.

$SU(3)_c$	Φ_Q, Ψ_Q	Φ_L, Ψ_L	Ψ, Φ
A	**3**	**1**	**1**
B	**1**	$\bar{\mathbf{3}}$	**3**

$SU(2)_L$	Φ_Q, Ψ_Q	Φ_L, Ψ_L	Ψ, Φ
I	**2**	**2**	**1**
II	**1**	**1**	**2**
III	**3**	**3**	**2**
IV	**2**	**2**	**3**
V	**3**	**1**	**2**
VI	**1**	**3**	**2**

$U(1)_Y$	Φ_Q, Ψ_Q	Φ_L, Ψ_L	Ψ, Φ
	$1/6 - X$	$-1/2 - X$	X

derived from gauge invariance as shown in the last line of Table I.

The resulting combinations of quantum numbers are shown in Tables II and III, which collect the possible models with, respectively, a fermion and a scalar flavor mediator. The models have been labeled according to the spin of the flavor mediator ($\mathcal{F}$ or $\mathcal{S}$), the combination of $SU(2)_L$ and $SU(2)_c$ representations of the fields as given in Table I and—for categories containing more than one model—the hypercharge of the flavor mediator. The tables include only models featuring at least a viable DM candidate, i.e., an electrically neutral stable state. The representation to which this state belongs has been marked with *. Notice that the DM candidate can belong to any of the three NP fields for both classes of models.

DM candidates with nonzero hypercharge are severely constrained by the direct detection experiments, as a consequence of the coherently enhanced spin independent (SI) interactions with nuclei mediated by the Z boson. To keep the particle content of our models minimal, we only consider fermion DM candidates with $Y = 0$.[2] Instead, if DM belongs to a scalar multiplet one can evade the direct detection bounds by introducing a suitable mass splitting between CP-odd and CP-even components through couplings of the scalar potential. Since this avoids the

---

[2]Scenarios with Dirac fermion DM and $Y \neq 0$ would be still viable if the field content of the model is extended beyond our minimality criterion, such that the DM field mixes with an additional Majorana fermion making the lightest state Majorana; see, e.g., Refs. [59,60]. This is the well-known case of the supersymmetric Higgsinos, $SU(2)_L$ doublet fermions mixing with a Majorana singlet (the Bino), and a Majorana triplet (the Wino).

TABLE II. Models with a fermion flavor mediator (Class $\mathcal{F}$). The fields are denoted by their transformation properties under, respectively, $[SU(3)_c, SU(2)_L, U(1)_Y]$. We highlight in bold the models that we study in detail in Sec. IV.

Label	Φ_Q	Φ_L	Ψ
$\mathcal{F}_{\text{IA};-1}$	$(\mathbf{3},\mathbf{2},7/6)$	$(\mathbf{1},\mathbf{2},1/2)^\star$	$(\mathbf{1},\mathbf{1},-1)$
$\boldsymbol{\mathcal{F}_{\text{IA};0}}$	$(\mathbf{3},\mathbf{2},1/6)$	$(\mathbf{1},\mathbf{2},-1/2)^\star$	$(\mathbf{1},\mathbf{1},0)^\star$
$\boldsymbol{\mathcal{F}_{\text{IB};-1/3}}$	$(\mathbf{1},\mathbf{2},1/2)^\star$	$(\bar{\mathbf{3}},\mathbf{2},-1/6)$	$(\mathbf{3},\mathbf{1},-1/3)$
$\mathcal{F}_{\text{IB};2/3}$	$(\mathbf{1},\mathbf{2},-1/2)^\star$	$(\bar{\mathbf{3}},\mathbf{2},-7/6)$	$(\mathbf{3},\mathbf{1},2/3)$
$\mathcal{F}_{\text{IIA}}$	$(\mathbf{3},\mathbf{1},2/3)$	$(\mathbf{1},\mathbf{1},0)^\star$	$(\mathbf{1},\mathbf{2},-1/2)$
$\mathcal{F}_{\text{IIB}}$	$(\mathbf{1},\mathbf{1},0)^\star$	$(\bar{\mathbf{3}},\mathbf{1},-2/3)$	$(\mathbf{3},\mathbf{2},1/6)$
$\mathcal{F}_{\text{IIIA};-3/2}$	$(\mathbf{3},\mathbf{3},5/3)$	$(\mathbf{1},\mathbf{3},1)^\star$	$(\mathbf{1},\mathbf{2},-3/2)$
$\boldsymbol{\mathcal{F}_{\text{IIIA};-1/2}}$	$(\mathbf{3},\mathbf{3},2/3)$	$(\mathbf{1},\mathbf{3},0)^\star$	$(\mathbf{1},\mathbf{2},-1/2)$
$\mathcal{F}_{\text{IIIA};1/2}$	$(\mathbf{3},\mathbf{3},-1/3)$	$(\mathbf{1},\mathbf{3},-1)^\star$	$(\mathbf{1},\mathbf{2},1/2)$
$\mathcal{F}_{\text{IIIB};-5/6}$	$(\mathbf{1},\mathbf{3},1)^\star$	$(\bar{\mathbf{3}},\mathbf{3},1/3)$	$(\mathbf{3},\mathbf{2},-5/6)$
$\mathcal{F}_{\text{IIIB};1/6}$	$(\mathbf{1},\mathbf{3},0)^\star$	$(\bar{\mathbf{3}},\mathbf{3},-2/3)$	$(\mathbf{3},\mathbf{2},1/6)$
$\mathcal{F}_{\text{IIIB};7/6}$	$(\mathbf{1},\mathbf{3},-1)^\star$	$(\bar{\mathbf{3}},\mathbf{3},-5/3)$	$(\mathbf{3},\mathbf{2},7/6)$
$\mathcal{F}_{\text{IVA};-1}$	$(\mathbf{3},\mathbf{2},7/6)$	$(\mathbf{1},\mathbf{2},1/2)^\star$	$(\mathbf{1},\mathbf{3},-1)$
$\mathcal{F}_{\text{IVA};0}$	$(\mathbf{3},\mathbf{2},1/6)$	$(\mathbf{1},\mathbf{2},-1/2)^\star$	$(\mathbf{1},\mathbf{3},0)^\star$
$\mathcal{F}_{\text{IVB};-1/3}$	$(\mathbf{1},\mathbf{2},1/2)^\star$	$(\bar{\mathbf{3}},\mathbf{2},-1/6)$	$(\mathbf{3},\mathbf{3},-1/3)$
$\mathcal{F}_{\text{IVB};2/3}$	$(\mathbf{1},\mathbf{2},-1/2)^\star$	$(\bar{\mathbf{3}},\mathbf{2},-7/6)$	$(\mathbf{3},\mathbf{3},2/3)$
$\mathcal{F}_{\text{VA}}$	$(\mathbf{3},\mathbf{3},2/3)$	$(\mathbf{1},\mathbf{1},0)^\star$	$(\mathbf{1},\mathbf{2},-1/2)$
$\mathcal{F}_{\text{VB};-5/6}$	$(\mathbf{1},\mathbf{3},1)^\star$	$(\bar{\mathbf{3}},\mathbf{1},1/3)$	$(\mathbf{3},\mathbf{2},-5/6)$
$\mathcal{F}_{\text{VB};1/6}$	$(\mathbf{1},\mathbf{3},0)^\star$	$(\bar{\mathbf{3}},\mathbf{1},-2/3)$	$(\mathbf{3},\mathbf{2},1/6)$
$\mathcal{F}_{\text{VB};7/6}$	$(\mathbf{1},\mathbf{3},-1)^\star$	$(\bar{\mathbf{3}},\mathbf{1},-5/3)$	$(\mathbf{3},\mathbf{2},7/6)$
$\mathcal{F}_{\text{VIA};-3/2}$	$(\mathbf{3},\mathbf{1},5/3)$	$(\mathbf{1},\mathbf{3},1)^\star$	$(\mathbf{1},\mathbf{2},-3/2)$
$\mathcal{F}_{\text{VIA};-1/2}$	$(\mathbf{3},\mathbf{1},2/3)$	$(\mathbf{1},\mathbf{3},0)^\star$	$(\mathbf{1},\mathbf{2},-1/2)$
$\mathcal{F}_{\text{VIA};1/2}$	$(\mathbf{3},\mathbf{1},-1/3)$	$(\mathbf{1},\mathbf{3},-1)^\star$	$(\mathbf{1},\mathbf{2},1/2)$
$\mathcal{F}_{\text{VIB}}$	$(\mathbf{1},\mathbf{1},0)^\star$	$(\bar{\mathbf{3}},\mathbf{3},-2/3)$	$(\mathbf{3},\mathbf{2},1/6)$

TABLE III. Same as Table II for models with a scalar flavor mediator (Class $\mathcal{S}$).

Label	Ψ_Q	Ψ_L	Φ
$\boldsymbol{\mathcal{S}_{\text{IA}}}$	$(\mathbf{3},\mathbf{2},1/6)$	$(\mathbf{1},\mathbf{2},-1/2)$	$(\mathbf{1},\mathbf{1},0)^\star$
$\mathcal{S}_{\text{IIA};-1/2}$	$(\mathbf{3},\mathbf{1},2/3)$	$(\mathbf{1},\mathbf{1},0)^\star$	$(\mathbf{1},\mathbf{2},-1/2)^\star$
$\mathcal{S}_{\text{IIA};1/2}$	$(\mathbf{3},\mathbf{1},-1/3)$	$(\mathbf{1},\mathbf{1},-1)$	$(\mathbf{1},\mathbf{2},1/2)^\star$
$\boldsymbol{\mathcal{S}_{\text{IIB}}}$	$(\mathbf{1},\mathbf{1},0)^\star$	$(\bar{\mathbf{3}},\mathbf{1},-2/3)$	$(\mathbf{3},\mathbf{2},1/6)$
$\boldsymbol{\mathcal{S}_{\text{IIIA};-1/2}}$	$(\mathbf{3},\mathbf{3},2/3)$	$(\mathbf{1},\mathbf{3},0)^\star$	$(\mathbf{1},\mathbf{2},-1/2)^\star$
$\mathcal{S}_{\text{IIIA};1/2}$	$(\mathbf{3},\mathbf{3},-1/3)$	$(\mathbf{1},\mathbf{3},-1)$	$(\mathbf{1},\mathbf{2},1/2)^\star$
$\mathcal{S}_{\text{IIIB}}$	$(\mathbf{1},\mathbf{3},0)^\star$	$(\bar{\mathbf{3}},\mathbf{3},-2/3)$	$(\mathbf{3},\mathbf{2},1/6)$
$\mathcal{S}_{\text{IVA};-1}$	$(\mathbf{3},\mathbf{2},7/6)$	$(\mathbf{1},\mathbf{2},1/2)$	$(\mathbf{1},\mathbf{3},-1)^\star$
$\mathcal{S}_{\text{IVA};0}$	$(\mathbf{3},\mathbf{2},1/6)$	$(\mathbf{1},\mathbf{2},-1/2)$	$(\mathbf{1},\mathbf{3},0)^\star$
$\mathcal{S}_{\text{IVA};1}$	$(\mathbf{3},\mathbf{2},-5/6)$	$(\mathbf{1},\mathbf{2},-3/2)$	$(\mathbf{1},\mathbf{3},1)^\star$
$\mathcal{S}_{\text{VA};-1/2}$	$(\mathbf{3},\mathbf{3},2/3)$	$(\mathbf{1},\mathbf{1},0)^\star$	$(\mathbf{1},\mathbf{2},-1/2)^\star$
$\mathcal{S}_{\text{VA};1/2}$	$(\mathbf{3},\mathbf{3},-1/3)$	$(\mathbf{1},\mathbf{1},-1)$	$(\mathbf{1},\mathbf{2},1/2)^\star$
$\mathcal{S}_{\text{VB}}$	$(\mathbf{1},\mathbf{3},0)^\star$	$(\bar{\mathbf{3}},\mathbf{1},-2/3)$	$(\mathbf{3},\mathbf{2},1/6)$
$\mathcal{S}_{\text{VIA};-1/2}$	$(\mathbf{3},\mathbf{1},2/3)$	$(\mathbf{1},\mathbf{3},0)^\star$	$(\mathbf{1},\mathbf{2},-1/2)^\star$
$\mathcal{S}_{\text{VIA};1/2}$	$(\mathbf{3},\mathbf{1},-1/3)$	$(\mathbf{1},\mathbf{3},-1)$	$(\mathbf{1},\mathbf{2},1/2)^\star$
$\mathcal{S}_{\text{VIB}}$	$(\mathbf{1},\mathbf{1},0)^\star$	$(\bar{\mathbf{3}},\mathbf{3},-2/3)$	$(\mathbf{3},\mathbf{2},1/6)$

dangerous DM coupling to the Z without introducing more fields, we include in Tables II and III also solutions with DM belonging to scalar multiplets with $Y \neq 0$. Let us mention that some of the models included in the classification shown in Tables II and III were previously studied in the literature, namely, $\mathcal{F}_{\text{IA};0}$ [34], $\mathcal{F}_{\text{IIA}}$ [35], $\mathcal{S}_{\text{IA}}$ [30,33], $\mathcal{S}_{\text{IIA};-1/2}$ [31], and $\mathcal{S}_{\text{IIA};1/2}$ [32].

In the following sections, we will discuss in detail the different constraints (from flavor anomalies, LHC, relic density and direct detection) for the above-defined class of models.

III. STRATEGY

In this section we present the strategy that we are going to employ for each model under scrutiny. We take into account constraints coming from flavor physics, from the recasting of direct searches at the LHC and from DM searches. All these constraints are considered in a systematic and comprehensive way in order to assess whether, for a given model, a region of the parameter space where all bounds are evaded exists, or the model is excluded by the combination of all the constraints. We recall that the parameter space of each model is fully determined by three couplings plus three mass parameters, namely,

$$\{\Gamma_b^Q, \Gamma_s^Q, \Gamma_\mu^L\} \quad \text{plus} \quad \{M_\Psi, M_{\Phi_Q}, M_{\Phi_L}\}$$
$$\text{or plus} \quad \{M_\Phi, M_{\Psi_Q}, M_{\Psi_L}\} \tag{4}$$

for models with a fermion or a scalar flavor mediator, respectively.

A. Fit to flavor anomalies

The first step of our strategy consists in considering the constraints coming from flavor physics. In particular, we take into account data coming from the ratios R_K [2] and R_{K^*}

[3,4]—which are tests of LFU violation—from the angular analyses of the semi-leptonic decays $B \to K^{(*)} \ell^+ \ell^-$ [5–13] and $B_s \to \phi \ell^+ \ell^-$ [14], from the branching ratios of the fully leptonic decays $B_s \to \ell^+ \ell^-$ [61–64], and from the branching ratios of the radiative decays $B \to K^* \gamma$ [64], $B \to \phi \gamma$ [65], and $B \to X_s \gamma$ [64]. In order to systematically consider all the above experimental data, we directly rely on the constraints on the NP contributions to the Wilson coefficients (WC) of the operators in Eq. (1) obtained by global fits performed on this full data set; see, e.g., Refs. [18–26]. As reference value, we will employ the 2σ range obtained in the fit in Ref. [25]:

$$-0.72 \le \delta C_\mu^9 = -\delta C_\mu^{10} \le -0.36, \quad (\text{at } 2\sigma). \tag{5}$$

Moreover, we also take into account the latest SM results [66,67] on the mass difference of the neutral B_s mesons ΔM_s [64]:

$$\frac{\Delta M_s^{\text{SM}}}{\Delta M_s^{\text{exp}}} = 1.04_{-0.07}^{+0.04}. \tag{6}$$

In a similar fashion to what we did for $b \to s \ell \ell$ transitions, we can translate the experimental result, Eq. (6), into a bound NP to WC: introducing the effective $\Delta B = 2$ Hamiltonian

$$\mathcal{H}_{\text{eff}}^{B\bar{B}} \supset C^{B\bar{B}} (\bar{s} \gamma_\mu P_L b)(\bar{s} \gamma_\mu P_L b), \tag{7}$$

we can observe that the relation between the NP contribution to $C^{B\bar{B}}$ and ΔM_s reads

$$\frac{C^{B\bar{B}}}{C^{B\bar{B}} + \delta C^{B\bar{B}}} = \frac{\Delta M_s^{\text{SM}}}{\Delta M_s^{\text{exp}}} = 1.04_{-0.07}^{+0.04}. \tag{8}$$

In order to cast these constraints on the models described in the previous section, we recall that for each of the two classes of models defined in Eqs. (2)–(3) it is possible to write [28]

$$(\delta C_\mu^9)_{\mathcal{F}} = -(\delta C_\mu^{10})_{\mathcal{F}} = \frac{\sqrt{2}}{4 G_F V_{tb} V_{ts}^*} \frac{\Gamma_Q |\Gamma_\mu^L|^2}{32\pi \alpha_{\text{EM}} M_\Psi^2} (\eta F(x_Q, x_L) + 2\chi^M \eta^M G(x_Q, x_L)),$$

$$(\delta C_\mu^9)_{\mathcal{S}} = -(\delta C_\mu^{10})_{\mathcal{S}} = -\frac{\sqrt{2}}{4 G_F V_{tb} V_{ts}^*} \frac{\Gamma_Q |\Gamma_\mu^L|^2}{32\pi \alpha_{\text{EM}} M_\Phi^2} (\eta - \chi^M \eta^M) F(y_Q, y_L), \tag{9}$$

and

$$(\delta C^{B\bar{B}})_{\mathcal{F}} = \frac{\Gamma_Q^2}{128\pi^2 M_\Psi^2} (\eta_{BB} F(x_Q, x_L) + 2\chi^M \eta^M G(x_Q, x_L)),$$

$$(\delta C^{B\bar{B}})_{\mathcal{S}} = \frac{\Gamma_Q^2}{128\pi^2 M_\Phi^2} (\eta_{BB} - \chi^M \eta^M) F(y_Q, y_L), \tag{10}$$

where we have defined $\Gamma_Q \equiv \Gamma_b^Q \Gamma_s^{Q*}$ and we have introduced the compact notation $x_Q = M_{\Phi_Q}^2 / M_\Psi^2$, $x_L = M_{\Phi_L}^2 / M_\Psi^2$, and $y_Q = M_{\Psi_Q}^2 / M_\Phi^2$, $y_L = M_{\Psi_L}^2 / M_\Phi^2$, respectively. The

$SU(2)_L$ factors η, η^M, and η_{BB} are tabulated in Table IV, while the $SU(3)_c$ factor χ^M is equal to 1 only if Ψ (Φ) is a

TABLE IV. Table of the $SU(2)_L$-factors entering the Wilson coefficients in Eqs. (9) and (10).

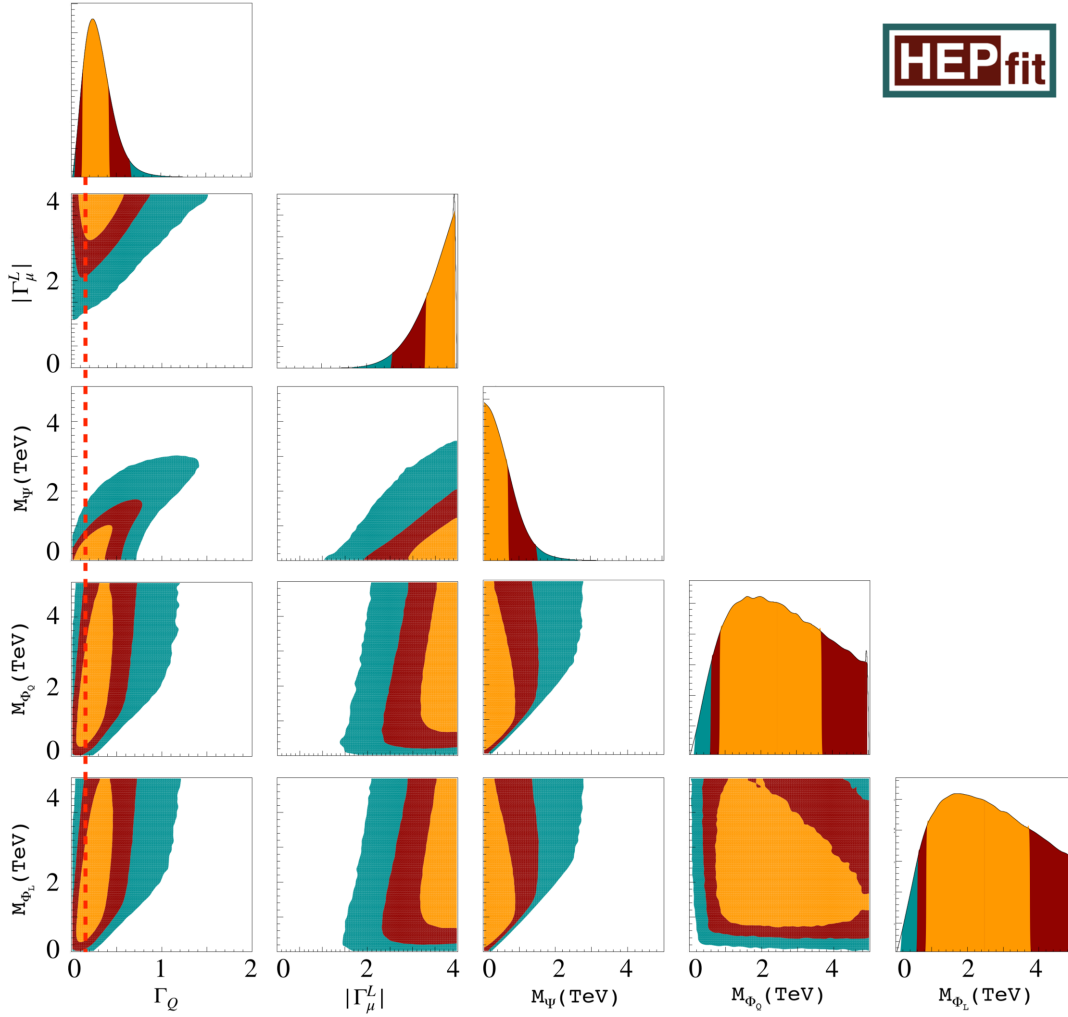| $SU(2)_L$	I	II	III	IV	V	VI
η	1	1	5/16	5/16	1/4	1/4
η^M	1	0	0	1/16	0	0
η_{BB}	1	1	5/16	5/16	5/16	1

FIG. 3.   Results of the flavor fit for the parameters $\Gamma_Q \equiv \Gamma_b^Q \Gamma_s^{Q*}$, $|\Gamma_\mu^L|$, M_Ψ, M_{Φ_Q}, and M_{Φ_L} in the scenario $\mathcal{F}_{\mathrm{IA};0}$ with Majorana DM. Both the 1D distribution for each of the five parameters and the 2D correlations between each of them are shown (with 1σ, 2σ and 3σ regions in orange, red, and blue, respectively). The red dashed line corresponds to the benchmark value $\tilde{\Gamma}_Q = 0.15$.

Majorana fermion (real scalar) in representation A of Table I, vanishing otherwise. Moreover, we have introduced the following loop functions:

$$F(x,y) = \frac{1}{(1-x)(1-y)} + \frac{x^2 \log x}{(1-x)^2(x-y)} + \frac{y^2 \log y}{(1-y)^2(y-x)},$$

$$G(x,y) = \frac{1}{(1-x)(1-y)} + \frac{x \log x}{(1-x)^2(x-y)} + \frac{y \log y}{(1-y)^2(y-x)}.$$

$$\tag{11}$$

The constraints in Eqs. (5) and (8) are exploited through a combined fit to the relevant set of parameters in Eq. (4) using the HEPfit package [68]. For each parameter, we adopt a flat prior with the following ranges:

(i) For the lepton coupling, we allow it to be in the range $|\Gamma_\mu^L| \in [0, 4]$. Regarding the quark coupling Γ_Q we first notice from Eq. (9) that, since the loop functions assume positive values for the mass regimes under

scrutiny, it is the only free parameter capable of affecting the sign of the Wilson coefficient; hence, in order to obtain the desired sign for δC_μ^9 according to Eq. (5) and remembering that $\mathrm{Re}(V_{ts}) < 0$, we allow it to be in the range $\Gamma_Q \in [0, 2]$ for models in class $\mathcal{F}$, and to be in the range $\Gamma_Q \in [-2, 0]$ for models in class $\mathcal{S}$; this choice will not affect the result for $\delta C^{B\bar{B}}$, since the coupling is squared in Eq. (10);

(ii) For the DM candidate mass, we require for it to be lighter than the other NP fields;

(iii) For the remaining NP masses, we let them vary up to 5 TeV.

The outcome of the fit is then summarized in terms of posterior probability distribution functions (PDFs) for each parameter, together with correlation plots between each pair of them.

As an example, we show in Fig. 3 the outcome of the fit to the model $\mathcal{F}_{\mathrm{IA};0}$, where the DM candidate is the

Majorana fermion Ψ. The diagonal of the triangle plot contains the 1D PDFs for the 5 parameters constrained by the model, while in the other panels we give the combined 2D PDFs showing the correlations among each couple of parameters. Let us now discuss the information we can extract from this result, since it will also be useful for the other models we consider in Sec. IV. Starting from the couplings 1D PDFs, we observe that Γ_Q is constrained to small values: this is a byproduct of the inclusion of ΔM_s in the fit, which disfavors higher values for this coupling. However, this implies that $|\Gamma_\mu^L|$ is pushed to values at the boundary of the perturbative region in order to satisfactory address the B anomalies. Concerning the masses 1D PDFs we first notice that the DM mass is allowed to grow only up to a few TeV due to the requirement that it has to be the lightest state of the NP sector. On the other hand, no upper bound can be inferred on the masses of the other NP fields, which are found to be unconstrained in the whole mass range under scrutiny. Moving on to the analysis of the combined 2D PDFs, we focus our attention on the first column of panels of Fig. 3, namely, the ones showing the correlations among Γ_Q and the other NP parameters included in the fit, where we have highlighted with a dashed red line the value $\Gamma_Q \sim 0.15$. From these panels it is indeed possible to infer that such value, sitting in the 1D PDFs of Γ_Q in the 1σ region and close to its mode, is an interesting benchmark point when looking also at the other parameters. Indeed, from the 2D PDFs describing the correlation among Γ_Q and $|\Gamma_\mu^L|$, we observe that this choice for the quark coupling implies that the 1σ and 2σ regions reach the lowest allowed values for the lepton coupling, corresponding to $|\Gamma_\mu^L| = 3$ and 2, respectively, with the 3σ bound reaching $|\Gamma_\mu^L| = 1$. Hence, the benchmark value $\Gamma_Q \sim 0.15$ is the one that better justifies the benchmark assignments $|\Gamma_\mu^L| = 1, 2, 3$, while a different value for the quark coupling would induce bigger values for the leptonic one. Finally, from the other 2D PDFs we observe that in correspondence to this benchmark value the 1σ (2σ) upper bound for M_{DM} is around 700 (1100) GeV, while for the other two fields the whole mass range is allowed at the 2σ level.

An analogous behavior for the posterior PDFs has been found in all the models analyzed in Sec. IV, with a value for $|\Gamma_Q| \sim 0.15$ (positive or negative, depending on whether the model belongs to class $\mathcal{F}$ or $\mathcal{S}$ respectively) such that the allowed 1σ and 2σ bounds on $|\Gamma_\mu^L|$ are the lowest, the 1σ and 2σ upper bounds for the DM mass are around 700 and 1100 GeV, respectively, and no upper bound is found at the 2σ level on the remaining masses. Therefore, in the following analysis we will fix the value for the quark coupling to the benchmark value $|\tilde{\Gamma}_Q| = 0.15$, and we will consider three different benchmark values for the leptonic coupling $|\Gamma_\mu^L| = 1, 2, 3$, corresponding to the 3σ, 2σ and 1σ lower bounds, respectively. Moreover, we observe that the

fit always allows us to fix the mass of one the two heavy NP partners of the DM candidate to be equal to 700 GeV (1100 GeV), the value corresponding to the 1σ (2σ) upper bound for the DM (which, being the lightest NP particle, obviously sets a lower bound on the rest of the spectrum).

Let us finish this subsection with a comment on another observable featuring a long-standing deviation from the SM prediction: the muon anomalous magnetic moment, $(g-2)_\mu$. Notice that the subset of our NP fields coupling to muons indeed contributes to the dipole operator responsible for $(g-2)_\mu$. Such a contribution is, however, chirally suppressed (our fields do not couple to right-handed muons), thus too small to account for the current $\sim 3.5\sigma$ discrepancy between SM prediction and experimental measurement [69], with the possible exception of tuned regions of the parameter space, as systematically discussed in [70]. A successful fit of the $(g-2)_\mu$ discrepancy would require the introduction of extra fields coupling to the SM Higgs field and thus providing a chiral enhancement to the muon dipole. Examples of such "next-to-minimal" dark matter scenarios naturally accounting for the $(g-2)_\mu$ discrepancy are given in [70,71] as well as, in combination with the B-physics anomalies, in [50,52].

B. LHC constraints

The second step of our strategy involves studying the bounds following from direct searches at the LHC. We will consider here as an example, without any loss of generality, the case where the flavor mediator is a scalar field (being the conclusions in the case of a fermion mediator identical). DM scenarios and LHC searches can be separated in two categories, depending on whether the DM candidate is the fermion field coupling to SM leptons (Ψ_L) or one of the two other possibilities (Ψ_Q or Φ).

(i) *Case 1.* If the DM candidate is either the field Ψ_Q or Φ, the main production channel at the LHC will be via QCD-mediated processes, such as

$$pp \to \Psi_Q \Psi_Q \to qq' + \not{E}_T, \quad \text{or}$$
$$pp \to \Phi\Phi \to qq' + \not{E}_T, \tag{12}$$

with DM being the field Φ or Ψ_Q, respectively, and appearing as missing energy in the detector. Here $q, q' = s, c, b, t$, that is, each of the quarks can be either a light quark, producing a jet, a bottom quark, producing a b jet, or a top quark, producing a b jet plus the products of the decay of the W boson.[3] Notice the similarity of this setup to simplified supersymmetric models with squarks decaying into neutralino DM. As a consequence, in order to produce exclusion plots in the (M_{Ψ_Q}, M_Φ) plane,

---

[3]Here and below, we are neglecting the production of u quarks, which are CKM suppressed.

it is possible to recast limits from LHC squark searches involving missing energy plus 2–6 jets, allowing also the presence of b jets. The latest of such analyses has been performed by CMS [72]. Let us stress once again that this recasting can be applied no matter which of the two NP fields in the couple $\{\Psi_Q, \Phi\}$ is the DM candidate, since the final states and, hence, the LHC signature is the same for both cases, as shown in Eq. (12).

In order to set bounds on M_{Ψ_L}, we now have to distinguish whether the DM candidate is the scalar Φ or the fermion Ψ_Q coupling to SM quarks. In the former case, one can constrain M_{Ψ_L} with a procedure analogous to the one outlined above: a pair of Ψ_L fields will be mainly produced by electroweak Drell-Yan, and they will subsequently decay into muons and DM, i.e., missing energy. Hence, this channel can be described as

$$pp \to \Psi_L \Psi_L \to \mu^+ \mu^- + E\!\!\!/_T. \qquad (13)$$

Therefore, similarly to what described above, in order to produce exclusion plots in the plane (M_{Ψ_L}, M_Φ) it is possible to recast limits from LHC slepton searches involving missing energy plus a muon pair. The latest of such analyses has been performed by ATLAS [73]. Moreover, there are also searches considering soft leptons performed by both ATLAS [74] and CMS [75]. In the second case (DM in Ψ_Q), on the other hand, Ψ_L does not couple directly to the DM candidate; hence, the above signature cannot be used. The main decay channel of the Ψ_L fields will consist instead of the cascade production of two muons plus two NP scalars Φ, which will further decay into quarks and DM candidates, i.e., missing energy. Hence, in this last scenario the signature will be

$$pp \to \Psi_L \Psi_L \to \mu^+ \mu^- + \Phi\Phi \to \mu^+ \mu^- + qq' + E\!\!\!/_T. \quad (14)$$

Therefore, in order to produce exclusion plots in the plane (M_{Ψ_L}, M_{Ψ_Q}), it is necessary to recast limits from combined LHC searches for stops cascade decaying into sleptons/charginos, involving missing energy plus 2 muons and 2–6 jets (including b jets). The latest of such analyses can be found in [76,77].

  (i) *Case 2.* If the DM candidate is the field Ψ_L, analogous considerations to the ones reported above Eq. (13) can be applied, with the signature reading now

$$pp \to \Phi\Phi \to \mu^+ \mu^- + E\!\!\!/_T. \qquad (15)$$

One can therefore use again the searches from Refs. [73–75] to constrain the plane (M_Φ, M_{Ψ_L}). Further, bounds on M_{Ψ_Q} can be obtained through the cascade decay

$$pp \to \Psi_Q \Psi_Q \to qq' + \Phi\Phi \to qq' + \mu^+ \mu^- + E\!\!\!/_T. \qquad (16)$$

Hence, exclusion plots in the plane (M_{Ψ_Q}, M_{Ψ_L}) can be obtained again by means of the analyses in [76,77].

While some combination of the above production and decay modes will appear in all models under study, there is a further collider signature that is possible if DM is part of an $SU(2)_L$ multiplet, where charged states will be also present. Because of electroweak radiative corrections, the charged states are typically $\mathcal{O}(100)$ MeV heavier than the neutral DM state [59,78,79]. Because of such a small mass splitting, the charged states—which can be pair produced through electroweak Drell-Yan at the LHC—are long lived, that is, they can travel a macroscopic distance (typically a few cm) in the detector before decaying (through the exchange of an off-shell W boson) into DM and a very soft and thus undetectable pion. The resulting signature is a so-called "disappearing-track" observable in the inner tracker of the detector. Searches for these kinds of events have been performed by both ATLAS [80] and CMS [81].

In order to exploit the LHC searches discussed above[4] we have implemented, as first step, the models in Feynrules 2.3 [82] in order to generate Universal Feynrules Output files, which are subsequently passed to MadGraph5_aMC@NLO 2.7[83] where the matrix elements are calculated and a set of 50k events is generated. The partonic events are showered using Pythia 8 [84], the detector effects are simulated by means of Delphes 3 [85], and the result is eventually passed to CheckMATE 2 [86], which compares the simulated signal with the experimental searches at the LHC and determines whether the model point is excluded at the 90% confidence level. For the LHC searches selected above that are not yet implemented in the current version of CheckMATE, we employ the AnalysisManager framework in order to define them ourselves [87].

As said above, such a procedure determines whether a model is excluded at the 90% confidence level for a fixed value of the six parameters $\bar{\Gamma}_b^Q$, $\bar{\Gamma}_s^Q$, $\bar{\Gamma}_\mu^L$, $\bar{M}_\Phi$, $\bar{M}_{\Psi_Q}$, and $\bar{M}_{\Psi_L}$. This means that, in order to produce an exclusion plot in the (M_{Ψ_Q}, M_Φ) plane [or in the (M_{Ψ_L}, M_Φ) one, if Ψ_L is the DM candidate], we have to fix the values of the three couplings and of the remaining mass to some set values. The chosen values for these four parameters will be guided by the benchmark values inferred from the flavor fit performed in the previous section. Regarding the lepton coupling, we can directly adopt one of the three benchmark

---

[4]The following procedure applies to the "prompt" signatures of Eqs. (12)–(15), while we will assess the bounds from disappearing tracks from existing literature, as explained in the following section for the models where these searches are relevant.

values inferred from the flavor fit, i.e., $|\Gamma_\mu^L| = 1, 2, 3$. However, the same cannot be done for the quark couplings since the flavor fit gave a benchmark value for the product $|\Gamma_b^Q \Gamma_s^{Q*}|$, i.e., $|\tilde{\Gamma}_Q| = 0.15$. On the other hand, LHC constraints are sensitive to the individual values to the two quark couplings and not only to their product. Hence, in the following we will inspect for each model two different benchmark cases:

$$\text{i) } |\bar{\Gamma}_b^Q| = 1, \qquad |\bar{\Gamma}_s^Q| = |\tilde{\Gamma}_Q|,$$

$$\text{ii) } |\bar{\Gamma}_b^Q| = |\bar{\Gamma}_s^Q| = \sqrt{|\tilde{\Gamma}_Q|}. \qquad (17)$$

We are now left to fix the value of one of the three masses. In the case where the DM is Ψ_L, we will fix the value of the mass of Ψ_Q, which is a colored particle not directly coupling to the DM candidate. The produced signature will be the cascade decay shown in Eq. (16), and hence we will have to rely on the recasting from Refs. [76,77]. We infer that (unless $M_{\Psi_Q} - M_{\Psi_L} \lesssim 50$ GeV) we have to consider as a benchmark value $M_{\Psi_Q} = 1400$ GeV. This is indeed the lowest allowed value for this parameter such that no lower bound is induced on the DM mass. In a similar fashion, if the DM candidate is Ψ_Q we will fix the mass of the colored field Ψ_L. Once again, given the signature of Eq. (14) we employ the recasting from Refs. [76,77] and obtain also for this field the benchmark value $M_{\Psi_L} = 1400$ GeV. Finally, if the flavor mediator Φ is the DM particle, the particle whose mass we will fix is yet again Ψ_L, but this field is now a color singlet directly coupling to the DM candidate. We can therefore directly employ the recasting from Refs. [73–75], and observe that we can set the mass of Ψ_L to one of the two benchmark values inferred from the flavor fit of the previous section, i.e., $M_{\Psi_L} = 700$ or 1100 GeV. Indeed, the highest excluded value from the recasting of such results is always found to be at most $\mathcal{O}(600)$ GeV.

Summarizing, given the above benchmark values for four parameters, it is possible to combine either in the (M_{Ψ_Q}, M_Φ) plane or in the (M_{Ψ_L}, M_Φ) one (according to whether the DM candidate is Ψ_Q or Φ, in the former case, or Ψ_L, in the latter). Indeed, the WC $\delta C_\mu^9 = -\delta C_\mu^{10}$ is simply a function of the two masses, once all the other parameters are fixed to benchmark values. Following the procedure outlined above it is therefore possible to visualize on the same plane both the region that can account for the flavor anomalies at the 2σ level as in Eq. (5), and the one excluded at 90% C.L. by our recasting of direct searches at LHC.

C. Constraints from DM phenomenology

As a last step, the flavor and LHC constraints can be complemented with the ones from DM phenomenology. Concerning the latter, the models considered here belong to the category of the so-called *t*-channel portals [88–95]

(a "flavored" variant of this kind of setup has been also considered here [96–100]). Our assumption that a good fit of the *B* anomalies is achieved introduces, however, some relevant variation in the phenomenology of these kinds of models, especially for what concerns direct detection.

As will be shown in the following, when some model parameters are fixed by the fit of flavor observables, the latter constraints can be easily visualized into two-dimensional mass-mass plots to compare the corresponding viable regions with those fulfilling the requirements from both LHC and flavor physics.

1. Relic density

The DM relic abundance has been measured with great precision by the Planck experiment [101] and it is represented by the parameter $\Omega_{\rm DM} h^2$ whose value is

$$\Omega_{\rm DM} h^2 = 0.1199 \pm 0.0022. \qquad (18)$$

As will be evident in the next sections, for values of the couplings compatible with flavor anomalies, the DM is capable of reaching thermal equilibrium in the early Universe and, hence, can achieve its final relic density through the freeze-out mechanism. In such a case, the DM abundance is the solution of a Boltzmann equation which can be written as [102,103]

$$\Omega_{\rm DM} h^2 \approx 8.76 \times 10^{-11} \text{ GeV}^{-2} \left[\int_{T_{\rm f.o.}}^{T_0} g_*^{1/2} \langle \sigma v \rangle_{\rm eff} \frac{dT}{M_{\rm DM}} \right]^{-1}, \qquad (19)$$

where $\langle \sigma v \rangle_{\rm eff}$ is the effective thermally averaged DM annihilation cross section including coannihilations and g_* is the effective number of relativistic degrees of freedom. The integral is computed between the freeze-out temperature $T_{\rm f.o.}$ (we recall that for WIMP $T_{\rm f.o.} \sim \frac{M_{\rm DM}}{20} - \frac{M_{\rm DM}}{30}$) and the current temperature of the Universe T_0. Defining M the field that is *t*-channel exchanged in DM pair annihilations and also contributes to coannihilation processes, the DM effective annihilation cross section can be written as [88]

$$\langle \sigma v \rangle_{\rm eff} = \frac{1}{2} \langle \sigma v \rangle_{\rm DM\,DM} \frac{g_{\rm DM}^2}{g_{\rm eff}^2}$$
$$+ \langle \sigma v \rangle_{\rm DM\,M} \frac{g_{\rm DM} g_{\rm M}}{g_{\rm eff}^2} (1 + \Delta)^{3/2} \exp[-x\Delta]$$
$$+ \frac{1}{2} \langle \sigma v \rangle_{\rm M^\dagger M} \frac{g_{\rm M}^2}{g_{\rm eff}^2} (1 + \Delta)^3 \exp[-2x\Delta], \qquad (20)$$

where $x = M_{\rm DM}/T$. $\langle \sigma v \rangle_{\rm DM\,DM}$ describes DM pair annihilation processes into SM fermions mediated by *t*-channel exchange of the field M. Given the assumptions stated in the previous sections, the possible final states are $\mu^+ \mu^-$, and

$\bar{q}q'$ where $q, q' = s, c, b, t$.[5] $\langle\sigma v\rangle_{\mathrm{DMM}}$ represents coannihilations processes with a DM and an M particle in the initial states while $\langle\sigma v\rangle_{\mathrm{M^\dagger M}}$ describes the contribution of M pair annihilation processes to the DM effective annihilation cross section provided that the mass splitting between DM and M is sufficiently small. Notice that the expression above is valid for complex-scalar and Dirac fermion DM. In the case of real scalar and Majorana DM we have a slightly different expression:

$$\langle\sigma v\rangle_{\mathrm{eff}} = \langle\sigma v\rangle_{\mathrm{DMDM}} \frac{g_{\mathrm{DM}}^2}{g_{\mathrm{eff}}^2}$$
$$+ \langle\sigma v\rangle_{\mathrm{DMM}} \frac{g_{\mathrm{DM}} g_{\mathrm{M}}}{g_{\mathrm{eff}}^2}(1+\Delta)^{3/2}\exp[-x\Delta]$$
$$+ (\langle\sigma v\rangle_{\mathrm{M^\dagger M}} + \langle\sigma v\rangle_{\mathrm{MM}}) \frac{g_{\mathrm{M}}^2}{g_{\mathrm{eff}}^2}(1+\Delta)^3\exp[-2x\Delta].$$

In the above equations $\Delta = (M_{\mathrm{M}} - M_{\mathrm{DM}})/M_{\mathrm{DM}}$ is the relative DM/mediator mass splitting while

$$g_{\mathrm{eff}} = g_{\mathrm{DM}} + g_{\mathrm{M}}(1+\Delta)^{3/2}\exp[-x\Delta], \qquad (21)$$

where g_{M} and g_{DM} are the internal degrees of freedom of the mediator and of the DM.

In our analysis, the DM relic density, including coannihilations, have been computed with great numerical precision through the package micrOMEGAs [37].[6] To clarify our results we provide nevertheless analytical expressions of the DM annihilation cross section into fermion pairs, the most relevant in the regions of parameter space favored by B anomalies (see below), at the leading order in the conventional velocity expansion (as further simplification we have neglected the masses of the final state fermions) [88–90,106]:

$$\langle\sigma v\rangle_{\mathrm{DMDM}}^{\mathrm{Complex}} = \sum_f N_c \frac{\lambda_f^4 M_{\Phi_{\mathrm{DM}}}^2 v^2}{48\pi(M_{\Phi_{\mathrm{DM}}}^2 + M_{F_f}^2)^2},$$

$$\langle\sigma v\rangle_{\mathrm{DMDM}}^{\mathrm{Real}} = \sum_f N_c \frac{\lambda_f^4 M_{\Phi_{\mathrm{DM}}}^6 v^4}{60\pi(M_{\Phi_{\mathrm{DM}}}^2 + M_{F_f}^2)^4},$$

$$\langle\sigma v\rangle_{\mathrm{DMDM}}^{\mathrm{Dirac}} = \sum_f N_c \frac{\lambda_f^4 M_{\Psi_{\mathrm{DM}}}^2}{32\pi(M_{\Psi_{\mathrm{DM}}}^2 + M_{S_f}^2)^4},$$

$$\langle\sigma v\rangle_{\mathrm{DMDM}}^{\mathrm{Majorana}} = \sum_f N_c \frac{\lambda_f^4 M_{\Psi_{\mathrm{DM}}}^2(M_{\Psi_{\mathrm{DM}}}^4 + M_{S_f}^4)v^2}{48\pi(M_{\Psi_{\mathrm{DM}}}^2 + M_{S_f}^2)^4}, \qquad (22)$$

where $N_c = 3(1)$ in the case of color-charged (color singlet) final state fermions. The sums run over the kinematically accessible final states, depending on the value of the DM mass.

The four expressions refer, as indicated, to real scalar, complex-scalar, Dirac fermion, and Majorana fermion DM. Scalar and fermionic DM candidates have been generically called Φ_{DM} and Ψ_{DM}, respectively, while the states exchanged in the t-channel Feynman diagrams and interacting with the fermion f have been called S_f and F_f. Finally, λ_f correspond to suitable assignments of $\Gamma_{\mu,s,b}^{L,Q}$ according to the final states.[7] While the four cross sections have a very similar mass dependence in the limit in which DM is much lighter than the NP field exchanged in the t channel, they feature a very different velocity dependence. We notice indeed that the annihilation cross section is s-wave dominated, in the case of Dirac fermion, p-wave

suppressed in the case of complex-scalar DM and Majorana fermion, and even further (d-wave) suppressed in the case of real scalar DM. Given that $v^2 \sim 0.1$, we expect that, while Dirac DM will easily comply with the requirement of the correct DM relic density, real scalar DM will, instead, be typically overabundant in light of its very suppressed annihilation cross section, unless the latter will be enhanced, e.g., by coannihilations.

Annihilations into SM fermion pairs and coannihilations mediated by M represent the main contribution to the DM relic density in the case where the DM belongs to an $SU(2)_L$ singlet. In the case where DM belongs to an $SU(2)_L$ multiplet, it can also annihilate, through gauge interactions, into W- and Z-boson pairs. The latter annihilation processes easily become the dominant contribution to DM pair annihilations since the corresponding annihilation rate is not suppressed by the mass of the field M. For DM masses above the TeV, such cross section is further increased by the so called Sommerfeld enhancement [107–110] as well as by bound state formation [111]. Additional coannihilation processes, due to other components of the DM multiplet, are present as well.

As will be clear from the following analysis, imposing the correct relic density, Eq. (18), translates into a very strong constraint, only marginally compatible with the flavor anomalies and other phenomenological bounds. For this reason we will just apply, through Eq. (19), an overclosure bound $\Omega_{\mathrm{DM}}h^2 \leq 0.12$. However, while

---

[5]Up quarks can also be annihilation final states. Their contribution to the DM relic density is, however, negligible because of the CKM suppression of the couplings.

[6]As recently shown, e.g., in [104,105], in the case of coannihilations between the DM and a colored field, additional effects, like thermal corrections, Sommerfeld enhancement, and bound state formation might be relevant. We postpone a discussion of these effects to future studies.

[7]Notice that a color-charged NP field might interact with different quark generations. The expression of the annihilation cross section might slightly change in this case.

requiring that thermal DM production does not exceed the observed relic density, we will also assume that our DM candidate always accounts for 100% of DM, including in the regions of the parameter space where it would be underabundant, as a consequence of some (unspecified) nonthermal DM production mechanism; see, e.g., [112,113].

2. Direct detection

The scattering of the DM with nucleons and nuclei, which is at the base of direct detection (DD), is typically described through effective four-field operators coupling pairs of DM

particles with SM quark or gluon pairs. For all the models considered in this work, the strongest constraints come from SI interactions. For our analysis we have adopted the world leading limits given by the XENON1T Collaboration [114]. How effective the resulting constraints are depends on the spin of the DM and, in the case of scalar DM, on whether the field is real or complex, while in the case of fermionic DM, on its Dirac rather than Majorana nature. In the following illustrative discussion, we focus for simplicity on the case in which the DM is an $SU(2)_L$ singlet.

In the case of complex-scalar DM, the effective Lagrangian for DD reads

$$\mathcal{L}_{\text{eff}}^{\text{Scalar},q} = \sum_{q=u,d} c^q (\Phi_{\text{DM}}^\dagger i\overset{\leftrightarrow}{\partial}_\mu \Phi_{\text{DM}}) \bar{q}\gamma^\mu q + \sum_{q=u,d,s} d^q M_q \Phi_{\text{DM}}^\dagger \Phi_{\text{DM}} \bar{q}q + d^g \frac{\alpha_s}{\pi} \Phi_{\text{DM}}^\dagger \Phi_{\text{DM}} G^{a\mu\nu} G_{\mu\nu}^a$$
$$+ \sum_{q=u,d,s} g_1^q \frac{\Phi_{\text{DM}}(i\partial^\mu)(i\partial^\nu)\Phi_{\text{DM}} \mathcal{O}_{\mu\nu}^q}{M_{\Phi_{\text{DM}}}^2} + g_1^g \frac{\Phi_{\text{DM}}(i\partial^\mu)(i\partial^\nu)\Phi_{\text{DM}} \mathcal{O}_{\mu\nu}^g}{M_{\Phi_{\text{DM}}}^2}, \tag{23}$$

where $\mathcal{O}_{\mu\nu}^q$ and $\mathcal{O}_{\mu\nu}^g$ are the twist-two operators:

$$\mathcal{O}_{\mu\nu}^q = \bar{q}i\left(\frac{D_\mu\gamma_\nu + D_\nu\gamma_\mu}{2} - \frac{1}{4}g_{\mu\nu}\slashed{D}\right)q,$$
$$\mathcal{O}_{\mu\nu}^g = G_\mu^{a\rho}G_{\nu\rho}^a - \frac{1}{4}g_{\mu\nu}G_{\rho\sigma}^a G^{a\rho\sigma}. \tag{24}$$

As we can see, the effective Lagrangian considers just interactions with light quarks ($q = u$, d, s) and gluons. This is because the typical energy scale for DM scattering

processes is of the order of 1 GeV and, hence, heavy quark flavors, c, b, t, are integrated out.

The coefficient c^q in Eq. (23) can be further decomposed as $c^q = c_{\text{tree}}^q + c_Z^q + c_\gamma^q + c_{\text{box}}^q$. Illustrative diagrams associated to these different contributions are shown in Fig. 4. Notice that the figure actually displays the case of fermionic DM, discussed in the following. However, topologically analogous diagrams can be also obtained for scalar DM, since as we will discuss below, the two cases share many similarities.
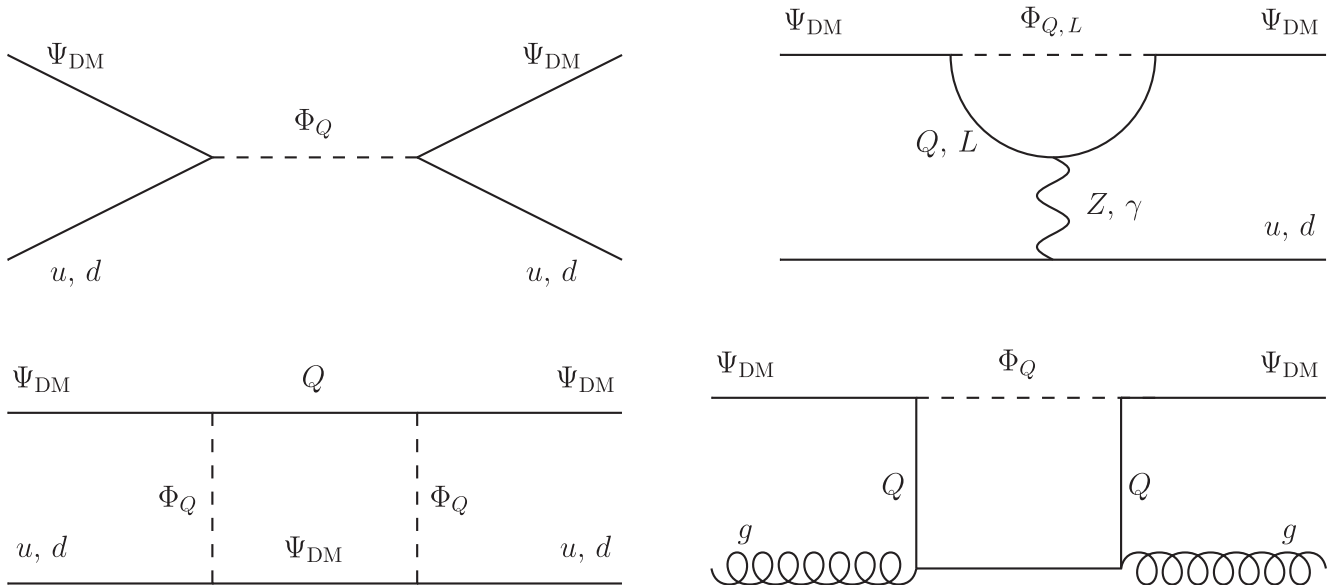

FIG. 4. Representative diagrams contributing to the DM-nucleon cross section relevant for direct detection experiments. For illustration, we only show some diagrams for the case of DM belonging to the fermionic flavor mediator Ψ. Analogous diagrams are present in the other cases (with the exception of models with DM belonging to Ψ_L/Φ_L where there is no tree-level diagram).

c_{tree}^q is the tree-level induced contribution from diagrams with the s-channel exchange of a color-charged scalar NP field. Since such a tree-level contribution describes the interactions of vector currents, the corresponding coefficient for the nucleons is just a linear combination of the contributions of the valence quarks, namely,

$$c_{\text{tree}}^p = 2c_{\text{tree}}^u + c_{\text{tree}}^d, \qquad c_{\text{tree}}^n = c_{\text{tree}}^u + 2c_{\text{tree}}^d. \qquad (25)$$

In the models considered in this work, the $c_{\text{tree}}^{N=p,n}$ coefficients are generated only by the CKM mixing. Having chosen a basis in which the down-type quark mass matrix is flavor diagonal we have

$$c_{\text{tree}}^u = \frac{(\Gamma_s^Q V_{us} + \Gamma_b^Q V_{ub})^2}{4(M_{\Phi_{\text{DM}}}^2 - M_{F_f}^2)}, \qquad c_{\text{tree}}^d = 0. \qquad (26)$$

Given this result, one cannot neglect *a priori* contributions from loop-level induced interactions. Indeed, the $c_{Z,\gamma}^q$ coefficients are generated by penguinlike diagrams as the ones shown in the second panel of Fig. 4, charged under the SM electroweak group, with SM γ and Z bosons while c_{box}^q is the coefficient associated to box diagrams analogous to the one present in the third panel of Fig. 4. The remaining operators in Eq. (23) arise, again at the loop level, from QCD interactions of the color-charged new fermions, possibly present in the theory [115]. Full analytical expressions for the $c_{Z,\gamma}^q$, c_{box}^q, $d^{q,g}$, $g_1^{q,g}$ can be found, e.g., in Refs. [30,115,116]. As will be discussed in the following, the strongest limits will arise from γ, Z penguins. We report here the relevant simplified expressions, as given in [30], in the limit $M_{\Phi_{\text{DM}}} \ll M_{F_f}$. For what concerns the γ penguin we have

$$c_\gamma^q \approx \frac{e^2 Q_q}{96\pi^2} \sum_{f=s,c,b,t,\mu} \frac{Q_f \lambda_f^2}{M_{F_f}^2} N_c \left[3 + \log\left(\frac{M_f^2}{M_{F_f}^2}\right)\right]. \qquad (27)$$

The coefficient associated to the Z penguin, in the same approximation, instead reads[8]

$$c_Z^q \approx v^q \frac{G_F}{\sqrt{2}} \sum_{f=s,c,b,t,\mu} \frac{\lambda_f^2 T_3^f N_c}{16\pi^2} \frac{M_f^2}{M_{F_l}^2} \left(\frac{3}{2} + \log\left(\frac{M_f^2}{M_{F_f}^2}\right)\right), \qquad (28)$$

where

$$v^u = \frac{8}{3}\sin^2\theta_W - 1, \qquad v^d = -\frac{4}{3}\sin^2\theta_W + 1. \qquad (29)$$

---

[8]In these expression, as well as the corresponding ones for fermionic DM, we have omitted for simplicity $O(1)$ factors that depend on the gauge quantum numbers of the field F_f (S_f for fermionic DM).

Among these two contributions, photon penguins give typically the dominant contribution with the exception of the case in which the effective coupling of the DM with top quarks is sizable, as a consequence of the enhancement proportional to the square of the top mass in c_Z^q.

The effective Lagrangian in Eq. (23) gives rise to the following scattering cross section for the DM over nucleons (for illustration we focus on the case of the proton):

$$\sigma_{\Phi_{\text{DM}}}^{\text{SI},p} = \frac{\mu_p^2}{\pi} \frac{[Zf_p + (A-Z)f_n]^2}{A^2}, \qquad (30)$$

where $\mu_p = M_{\Phi_{\text{DM}}} M_p / (M_{\Phi_{\text{DM}}} + M_p)$ is the DM/proton reduced mass. The extra factor depending on A, Z, being, respectively, the mass and atomic number of the detector material, allows a consistent comparison with experimental limits which assume equal coupling of the DM with protons and neutrons [117]. $f_{p,n}$ represent, in fact, the effective coupling of the DM with protons and neutrons and read

$$
\begin{aligned}
f_p &= c_{\text{tree}}^p + c_Z^p + c_\gamma^p + c_{\text{box}}^p \\
&\quad + M_p \sum_{q=u,d,s} \left(f_q^p d_q + \frac{3}{4}g_1^q(q(2) + \bar{q}(2))\right) \\
&\quad + \frac{3}{4} M_p \sum_{q=c,b,t} g_1^q G(2) - \frac{8}{9} f_{TG} f_G,
\end{aligned}
$$

$$
\begin{aligned}
f_n &= c_{\text{tree}}^n + c_Z^n + c_{\text{box}}^n + \frac{3}{4} M_n \sum_{q=u,d,s} (q(2) + \bar{q}(2))g_1^q \\
&\quad + \frac{3}{4} M_n \sum_{q=c,b,t} g_1^q G(2) - \frac{8}{9} f_{TG} f_G, \qquad (31)
\end{aligned}
$$

where $c_i^p = 2c_i^u + c_i^d$, $c_i^n = c_i^u + 2c_i^d$ with $i = $ tree, Z, γ, box, and $f_G = d_c^g + d_b^g + d_t^g$. The parameters $f_q^{N=n,p}$, f_{TG}, $q(2)$, and $G(2)$ are nucleon form factors defined as

$$\langle N|m_q \bar{q}q|N\rangle = M_N f_q^N, \qquad f_{TG} = 1 - \sum_{q=u,d,s} f_q^N,$$

$$\langle N|\mathcal{O}_{\mu\nu}^q|N\rangle = \frac{1}{M_N}\left(p_\mu p_\nu - \frac{1}{4}M_N^2 g_{\mu\nu}\right)(\bar{q}(2) + q(2)),$$

$$\langle N|\mathcal{O}_{\mu\nu}^g|N\rangle = \frac{1}{M_N}\left(p_\mu p_\nu - \frac{1}{4}M_N^2 g_{\mu\nu}\right)G(2). \qquad (32)$$

For our analysis we have used the default values implemented into the micrOMEGAs package [37].

It is important to remark that, contrary to the other coefficients, including the ones generated at the tree level, $c_{\gamma,Z}^p$ coefficients can be present in models in which the DM is coupled only to NP states charged under the electroweak gauge groups but that are color singlets.

If DM is a real scalar, the $\Phi_{\mathrm{DM}}^{\dagger} i \overleftrightarrow{\partial}_{\mu} \Phi_{\mathrm{DM}}$ operator identically vanishes. Hence, the DM direct detection cross section is expected to be suppressed.

Moving to fermionic DM, which we just call Ψ_{DM}, the effective Lagrangian for the Dirac case is

$$
\begin{aligned}
\mathcal{L}_{\mathrm{eff}}^{\mathrm{Dirac},q} = & \sum_{q=u,d} c^q \bar{\Psi}_{\mathrm{DM}} \gamma_\mu \Psi_{\mathrm{DM}} \bar{q} \gamma^\mu q + \sum_{q=u,d,s} d^q M_q \bar{\Psi}_{\mathrm{DM}} \Psi_{\mathrm{DM}} \bar{q} q + \sum_{q=c,b,t} d_q^g \frac{\alpha_s}{\pi} \bar{\Psi}_{\mathrm{DM}} \Psi_{\mathrm{DM}} G^{a\mu\nu} G_{\mu\nu}^a \\
& + \sum_{q=u,d,s} \left(g_1^q \frac{\bar{\Psi}_{\mathrm{DM}} i \partial^\mu \gamma^\nu \Psi_{\mathrm{DM}} \mathcal{O}_{\mu\nu}^q}{M_{\Psi_{\mathrm{DM}}}} + g_2^q \frac{\bar{\Psi}_{\mathrm{DM}} (i \partial^\mu)(i \partial^\nu) \Psi_{\mathrm{DM}} \mathcal{O}_{\mu\nu}^q}{M_{\Psi_{\mathrm{DM}}}^2} \right) \\
& + \sum_{q=c,b,t} \left(g_1^{g,q} \frac{\bar{\Psi}_{\mathrm{DM}} i \partial^\mu \gamma^\nu \Psi_{\mathrm{DM}} \mathcal{O}_{\mu\nu}^g}{M_{\Psi_{\mathrm{DM}}}} + g_2^{g,q} \frac{\bar{\Psi}_{\mathrm{DM}} (i \partial^\mu)(i \partial^\nu) \Psi_{\mathrm{DM}} \mathcal{O}_{\mu\nu}^g}{M_{\Psi_{\mathrm{DM}}}^2} \right).
\end{aligned}
\tag{33}
$$

Again, the coefficient c^q is a combination of CKM-suppressed tree-level and loop-induced contributions:

$$
c^q = c_{\mathrm{tree}}^q + c_Z^q + c_H^q + c_{\mathrm{box}}^q,
\tag{34}
$$

where, in contrast to the case of scalar DM, a contribution from Higgs penguin diagrams is present as well. The operator $\bar{\Psi}_{\mathrm{DM}} \gamma_\mu \Psi_{\mathrm{DM}} \bar{q} \gamma^\mu q$ behaves, with respect to direct detection, in an analogous way as $(\phi_{\mathrm{DM}}^{\dagger} i \overleftrightarrow{\partial}_{\mu} \phi_{\mathrm{DM}}) \bar{q} \gamma^\mu q$. So we have again that the coefficients $c^{p,n}$ at the nucleon level are linear combinations of the coefficients associated to up and down quarks. The coefficients $d^{q,g}$ can be decomposed into QCD contributions, which we label $d_{\mathrm{QCD}}^{q,g}$, analogous to the ones discussed for scalar DM, and a contribution from Higgs penguin diagrams, labeled as $d_H^{q,g}$. The coefficients $g_1^{g,q}$ finally come from QCD interactions mediated by quarks/gluons and possible NP color-charged states.

Effective interactions mediated by the photon are present as well. The latter are described, this time, by the following Lagrangian:

$$
\mathcal{L}_{\mathrm{eff}}^{\mathrm{Dirac},\gamma} = \frac{\tilde{b}_\Psi}{2} \bar{\Psi}_{\mathrm{DM}} \sigma^{\mu\nu} \Psi_{\mathrm{DM}} F_{\mu\nu} + b_\Psi \bar{\Psi}_{\mathrm{DM}} \gamma^\mu \Psi_{\mathrm{DM}} \partial^\nu F_{\mu\nu},
\tag{35}
$$

with the two terms dubbed, respectively, magnetic dipole moment and charge radius operators.

Concerning the relative contribution of the different coefficients, as already discussed in Ref. [118], the situation is analogous to the case of complex-scalar DM. The dominant contribution is typically associated to the charged radius and dipole operators, whose coefficient can be approximately written as

$$
\begin{aligned}
b_\psi &\approx -\frac{e}{48\pi M_{\Psi_{\mathrm{DM}}}^2} \sum_{f=s,c,b,t,\mu} N_c Q_f \lambda_f^2 \frac{M_{\Psi_{\mathrm{DM}}}^2}{M_{S_f}^2} \left(1 - 2\log\left(\frac{M_f^2}{M_{S_f}^2}\right) \right), \\
\tilde{b}_\psi &\approx -\frac{e}{8\pi M_{\Psi_{\mathrm{DM}}}} \sum_{f=s,c,b,t,\mu} N_c Q_f \lambda_f^2 \frac{M_{\Psi_{\mathrm{DM}}}^2 M_f^2}{M_{S_f}^2} \left(2 + \log\left(\frac{M_f^2}{M_{S_f}^2}\right) \right).
\end{aligned}
\tag{36}
$$

Again, in the case of sizable couplings of the DM with the top quark, the latter terms are overcome by c_Z^q which can be approximately written as

$$
c_Z^q = v^q \sum_{f=s,c,b,t,\mu} \frac{G_F}{\sqrt{2}} \frac{N_c \lambda_f^2}{32\pi^2} \frac{M_f^2}{M_{S_f}^2} \left(1 + \log\left(\frac{M_f^2}{M_{S_f}^2}\right) \right).
\tag{37}
$$

Given the presence of dipole operators, direct detection phenomenology is not fully caught by the scattering cross section over nucleons but, on the contrary, one has to rely on the DM scattering rate over nuclei:

$$
\frac{d\sigma}{dE_R} = \left(\frac{M_T}{2\pi v^2} |f^T|^2 + \alpha_{\mathrm{em}} \tilde{b}_\Psi^2 Z^2 \left(\frac{1}{E_R} - \frac{M_T}{2\mu_T^2 v^2} \right) \right) |F_{\mathrm{SI}}(E_R)|^2 + \tilde{b}_\Psi^2 \frac{\mu_T^2 M_T}{\pi v^2} \frac{J_T + 1}{3 J_T} |F_{\mathrm{D}}(E_R)|^2,
\tag{38}
$$

where

$$f^T = Zf_p + (A - Z)f_n, \tag{39}$$

and $\mu_T = M_{\Psi_{\mathrm{DM}}} M_T / (M_{\Psi_{\mathrm{DM}}} + M_T)$ with M_T being the mass of target nucleus. F_{SI} is the conventional SI nuclear form factor [119], while F_{D} is the form factor associated to dipole scattering [120]. Experimental limits have been obtained, in this case, with the procedure illustrated in Ref. [121].

In the case of Dirac DM, the coefficients f_p and f_n are written as

$$f_p = c^p_{\mathrm{tree}} + c^p_Z + c^p_{\mathrm{box}} - eb_\Psi - \frac{e\tilde{b}_\Psi}{2M_\Psi} + M_p \sum_{q=u,d,s} \left(f^p_q d_q + \frac{3}{4}(q(2) + \bar{q}(2))(g^q_1 + g^q_2) \right) + \frac{3}{4} M_p \sum_{q=c,b,t} G(2)(g^{g,q}_1 + g^{g,q}_2) - \frac{8}{9} f_{TG} f_G,$$

$$f_n = c^n_{\mathrm{tree}} + c^n_Z + c^n_H + c^n_{\mathrm{box}} + \frac{3}{4} M_n \sum_{q=u,d,s} (q(2) + \bar{q}(2))(g^q_1 + g^q_2) + \frac{3}{4} M_n \sum_{q=c,b,t} G(2)(g^{g,q}_1 + g^{g,q}_2) - \frac{8}{9} f_{TG} f_G. \tag{40}$$

Changing the nature of the DM, this time from Dirac to Majorana, leads to a markedly different case. Indeed, the $\bar{\Psi}\gamma^\mu\Psi$ and $\bar{\Psi}\sigma^{\mu\nu}\Psi$ operators are identically null and the DD phenomenology is again fully captured by the SI scattering cross section of the DM on protons:

$$\sigma^{\mathrm{SI},p}_{\Psi_{\mathrm{DM}}} = 4 \frac{\mu_p^2}{\pi} \frac{[Zf_p + (A - Z)f_n]^2}{A^2}, \tag{41}$$

where $f_{p,n}$ are defined analogously to Eq. (40).

In the case in which the DM belongs to an $SU(2)_L$ multiplet, no new operators are generated in the Lagrangians in Eqs. (23) and (33). The coefficients of the effective operators get, however, additional contributions from loop diagrams in which Z, W bosons are exchanged. The case of Majorana DM has been discussed extensively, e.g., in Refs. [60,122], while the case of real DM has been considered, to a lower extent, e.g., in Ref. [115]. To our knowledge, no analogous computations are available for complex-scalar and Dirac fermionic DM.

3. Indirect detection

As is well known, indirect detection (ID) for WIMPs relies on the search for the products of residual annihilation processes for DM occurring at present times. Similarly to the case of direct detection, it is convenient to distinguish the cases in which the DM is an $SU(2)_L$ singlet or not. In the former case, the main annihilation channels to consider are the ones into SM fermion pair final states. These lead mostly to continuous γ-ray signals which, for the ranges of DM masses considered in this work, can be probed by telescopes such as Fermi-LAT [123,124]. The impact of the resulting constraints is highly model dependent though. Indeed, having in mind the velocity expansion:

$$\langle \sigma v \rangle \approx a + bv^2, \tag{42}$$

we have that only for the s-wave dominated annihilation cross section, i.e., $a \neq 0$, are the values of the cross-section at

thermal freeze-out and present times comparable, so that eventual ID limits are effective. On the contrary, p wave, i.e., the b coefficient is the leading contribution, and dominated cross sections are affected by ID to a negligible extent. Notice as well that coannihilations are also mostly effective at thermal freeze-out while their rates are, instead, exponentially suppressed at present times. Given this, among the models presented in this work, only scenarios with Dirac fermionic DM can be probed by indirect detection.[9]

Summarizing, in the following section we will apply the strategy here described to several models of interest, in order to study whether such models allow for a region of the parameter space where all the constraints here described are evaded, or the model is excluded by the combination of all the constraints.

IV. RESULTS AND DISCUSSION

In this section, we analyze some of the models listed in Tables II and III, following the strategy illustrated in the previous section. Such models have been highlighted in bold in the tables. Our selection covers a broad variety of cases, including both scalar and fermion flavor mediators, as well as both scalar and fermion DM. Furthermore, we will separately discuss, where appropriate, both real and complex-scalar DM as well as both the Dirac and Majorana nature for fermionic DM. Finally, notice that our selection comprises models where DM is pure SM singlets as well as cases where it belongs to $SU(2)_L$ multiplets.

We will write for each model the Lagrangian responsible for the phenomenology we are interested in, according to the quantum numbers of the NP particles, and determine the regions of parameter space for which the B anomalies are accounted for. We will then combine this requirement with the constraints from collider searches of the NP particles as well as from DM phenomenology, in particular, relic density and direct detection. As discussed in Sec. III C 1, we will

---

[9]Notice that also for Majorana DM, $a \neq 0$. However, this term is helicity suppressed and, hence, typically subdominant with respect to the p-wave contribution.
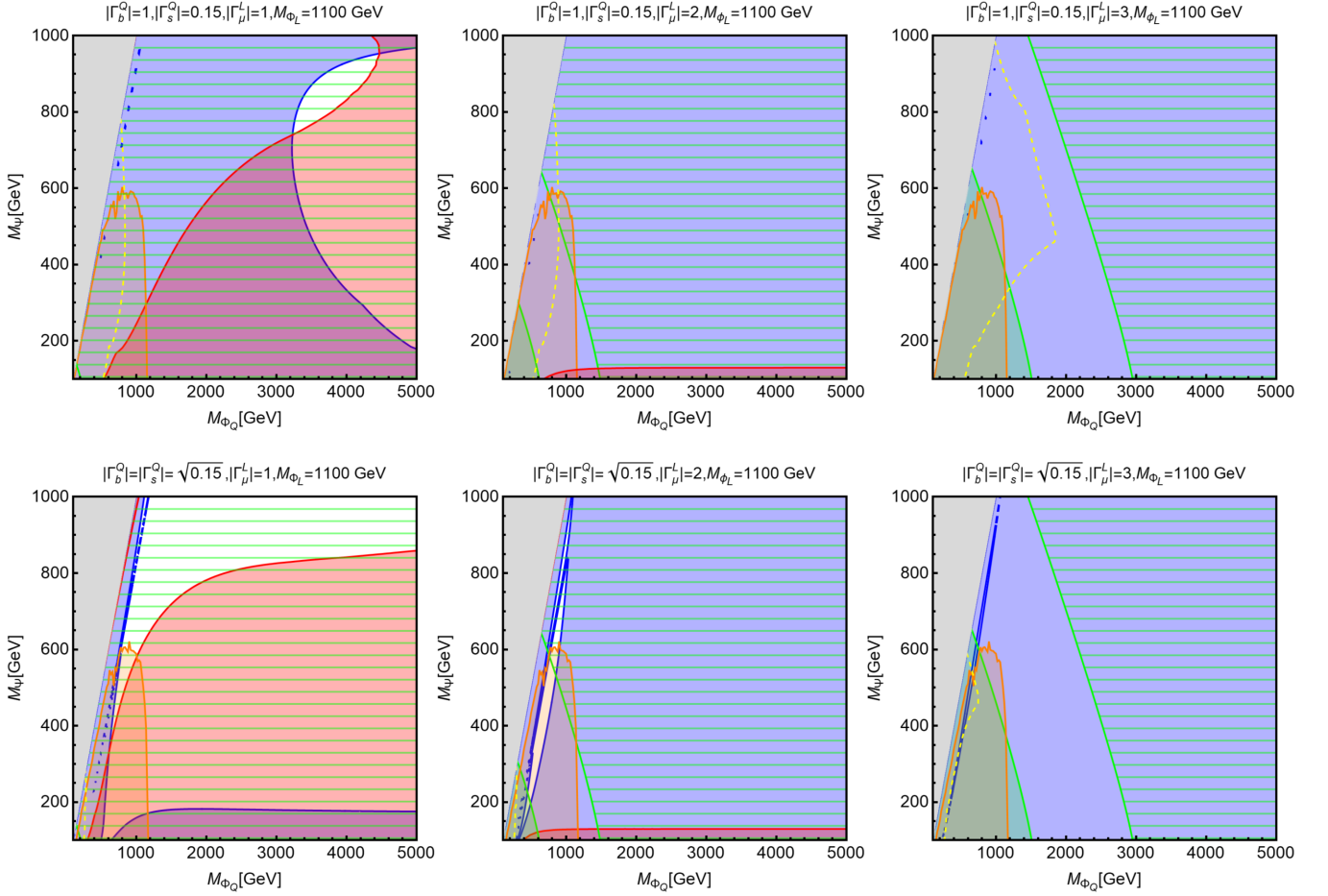
FIG. 5. Summary of the constraints for the model $\mathcal{F}_{\mathrm{IA};0}$ with Dirac dark matter. The first row corresponds to the benchmark case (i), with $|\Gamma_b^Q| = 1$, $|\Gamma_s^Q| = 0.15$, while in the second row we show the benchmark case (ii), with $|\Gamma_b^Q| = |\Gamma_s^Q| = \sqrt{0.15}$. For both cases we set $M_{\Phi_L} = 1100$ GeV and we show the three assignments $|\Gamma_\mu^L| = 1, 2, 3$. Regions outside green contours are not compatible with the *B* anomalies, with the solid green regions being strictly ruled out while the hatched green ones corresponding to contributions to $\delta C_\mu^{9,10}$ are not significantly deviating from the SM predictions, and are, hence, not strictly ruled out as the anomalies are still awaiting full experimental confirmation. The orange region represents the exclusion from direct searches at the LHC (see the text for details). Red regions are excluded because they correspond to overproduction of DM compared to the observed relic density. Blue regions are excluded by DD, while regions at the left of the yellow dashed contour are excluded by ID.

assume that in the regions of the parameter space where thermal DM production is insufficient some nonthermal mechanism is at work such that our DM candidate always accounts for 100% of the observed DM abundance.

A. $\mathcal{F}_{\mathrm{IA};0}$, Dirac singlet DM

We start considering the model $\mathcal{F}_{\mathrm{IA};0}$ with a singlet Dirac DM. This case, which is among the simplest in Tables II and III, has never been studied before and, as we will see, is subject to strong constraints. It is a good example to illustrate how bounds from different sources can altogether exclude a model. The Lagrangian of this model reads

$$\mathcal{L}_{\mathrm{int}} = \Gamma_i^Q \bar{Q}_i P_R \Psi \Phi_Q + \Gamma_i^L \bar{L}_i P_R \Psi \Phi_L + \text{H.c.}, \quad (43)$$

with the fields Φ_Q, Φ_L, and Ψ carrying, respectively, the following $SU(3)_c \otimes SU(2)_L \otimes U(1)_Y$ quantum numbers: $(\mathbf{3}, \mathbf{2}, 1/6)$, $(\mathbf{1}, \mathbf{2}, -1/2)$, and $(\mathbf{1}, \mathbf{1}, 0)$. As mentioned above, the DM candidate is the Dirac field $\Psi_{\mathrm{DM}} = \Psi$, which also plays the role of the flavor mediator in the diagram in Fig. 1. This scenario has been selected for our analysis since it features the highest degree of correlation. Indeed, notice that the DM field couples to both the NP fields Φ_Q and Φ_L, which are charged under the SM gauge group. Consequently, all the three couplings Γ_s^Q, Γ_b^Q, Γ_μ^L, entering $\delta C_\mu^{9,10}$ are, as well, contributing to the DM annihilation and scattering rates. For this reason we will also investigate, in the following, similar models with the Majorana fermion and scalar DM.

The results of our analysis for this model are presented in Fig. 5, displayed in the (M_Ψ, M_{Φ_Q}) two-dimensional plane. The two rows in the figure correspond to the two different

assignments of the couplings $[|\Gamma_s^Q|, |\Gamma_b^Q|)$, dubbed $i]$, $[|\Gamma_s^Q| = 1, |\Gamma_b^Q| = 0.15)$ and $ii]$, $(|\Gamma_s^Q| = |\Gamma_b^Q| = \sqrt{0.15})$, which proved to provide an equally good fit of the B anomalies, cf. Sec. III A. For each coupling configuration we show only one of our benchmark values for M_{Φ_L}, namely, 1100 GeV, and three values of $|\Gamma_\mu^L|$.

In each plot, the region compatible with the flavor anomalies is the one enclosed within the two green contours. As can be seen from the different filling styles, the regions outside these bands should be interpreted differently. Indeed, the regions on the left of the green contours (filled in green) are ruled out, since they correspond to the case in which $\delta C_\mu^{9,10}$ exceed the experimental limits. On the right of the contours, on the contrary, NP contributions to $C_\mu^{9,10}$ are increasingly suppressed so that these observables do not deviate, to a statistically relevant extent, with respect to the SM expectation. While current flavor anomalies are not reproduced in the latter parameter regions, we cannot strictly regard them as ruled out as the anomalies are still awaiting full experimental confirmation. These regions are denoted by a green horizontal hatching.

The orange region represents the exclusion from LHC searches for the signatures with jets and/or muons and missing energy described in Sec. III B. For this model, we show our recasting of the bound from Ref. [72] on $pp \to \Phi_Q \Phi_Q \to qq' + \Psi_{DM} \Psi_{DM}$.

Moving to DM phenomenology, the constraints from DM relic density are represented as red regions. As already mentioned, throughout our study we will just require that the value of $\Omega_{DM} h^2$, determined by applying the conventional thermal freeze-out paradigm, does not exceed the experimental determination, namely, $\Omega_{DM} h^2 \leq 0.12$. In each plot, the region of parameter space that does not fulfill this constraint has been marked in red. Being the DM a SM singlet, its relic density is determined, with the exception of the coannihilation region, by annihilations into SM fermion pairs. As the value of Γ_μ^L increases, the region with overabundant DM progressively reduces and, for $\Gamma_\mu^L = 3$, the DM is always underabundant within the whole range of M_Ψ and M_{Φ_Q}, shown in the plot. The blue region corresponds, instead, to the case in which the DM interactions with nuclei, as given by Eq. (38), exceed the constraints from XENON1T. Finally, with Dirac fermion DM, constraints from indirect detection should be taken also into account. The regions of parameter space at the left side of the dashed yellow contour are excluded by the latter types of searches.

As evident, in all the plots the region compatible with the flavor anomalies falls at least into one of the experimental exclusions. Among them, the strongest by far comes from direct detection, which excludes the whole range of masses considered in the different plots, besides the case $\Gamma_\mu^L = 1$: with such an assignment, only a region with $M_{\Phi_Q} = 4$–5 TeV survives in case (i), while a broader area is allowed in case (ii). Nevertheless, in these the NP contribution $\delta C_\mu^9 = -\delta C_\mu^{10}$ is too small to account for the observed anomalies. The direct detection bound extends even beyond multi-TeV masses for the Φ_Q field because it is actually saturated by the charge radius and magnetic dipole operators in Eq. (38) which are dominated by the contribution of the color singlet field M_{Φ_L}, whose mass and coupling Γ_μ^L were kept fixed in the analysis. The case $M_{\Phi_L} = 1.1$ TeV is hence ruled out by DM DD regardless of the assignment of the other parameters. For the same reasons we have shown no plot for $M_{\Phi_L} = 700$ GeV since, in such a case, the case $\Gamma_\mu^L = 1$ would also be completely ruled out by direct detection.

B. $\mathcal{F}_{IA;0}$, Majorana singlet DM

In this subsection we study the same model discussed in the previous one, defined by the Lagrangian in Eq. (43). The only difference is the nature of the DM field Ψ, now corresponding to a Majorana fermion. As pointed out above, this kind of scenario is particularly interesting since it features the highest degree of correlations between B anomalies and the other phenomenological observables considered in the present study. A model analogous to $\mathcal{F}_{IA;0}$ with Majorana DM has been already studied in Ref. [34]. The analysis in the latter reference differs from the present work in the fact that they strictly imposed the requirement of the correct relic density and used it to fix M_{Φ_L} as a function of the other parameters, in particular, the coupling Γ_μ^L. Furthermore, the latter parameter has been allowed to reach the perturbativity bound $\Gamma_\mu^L = \sqrt{4\pi}$. As already mentioned, we adopt here a more conservative approach for what concerns the DM relic density, keeping M_{Φ_L} and Γ_μ^L as free parameters in the fit of flavor observables and considering $\Gamma_\mu^L \leq 3$ in our phenomenological study. Given these different assumptions, our findings slightly differ from the ones reported in Ref. [34].

We repeat the analysis whose procedure has been illustrated in detail in the previous section. The results are shown in Figs. 6 and 7. As we can see, we find a very different picture with respect to the results of the previous case as shown in Fig. 5. This is a consequence of the different nature of the fermionic DM candidate. One can indeed find regions of the parameter space compatible with the flavor anomalies and not in tension with other experimental bounds, even for the lighter benchmark value $M_{\phi_L} = 700$ GeV. For $\Gamma_\mu^L \gtrsim 2$ it is also possible to have, albeit in a narrow window of the parameter space, a good fit of the flavor anomalies and, simultaneously, saturate the observed DM relic density ($\Omega_{DM} h^2 \simeq 0.12$) with a standard thermal WIMP. This occurs for DM masses between approximately 50 and 150 GeV.

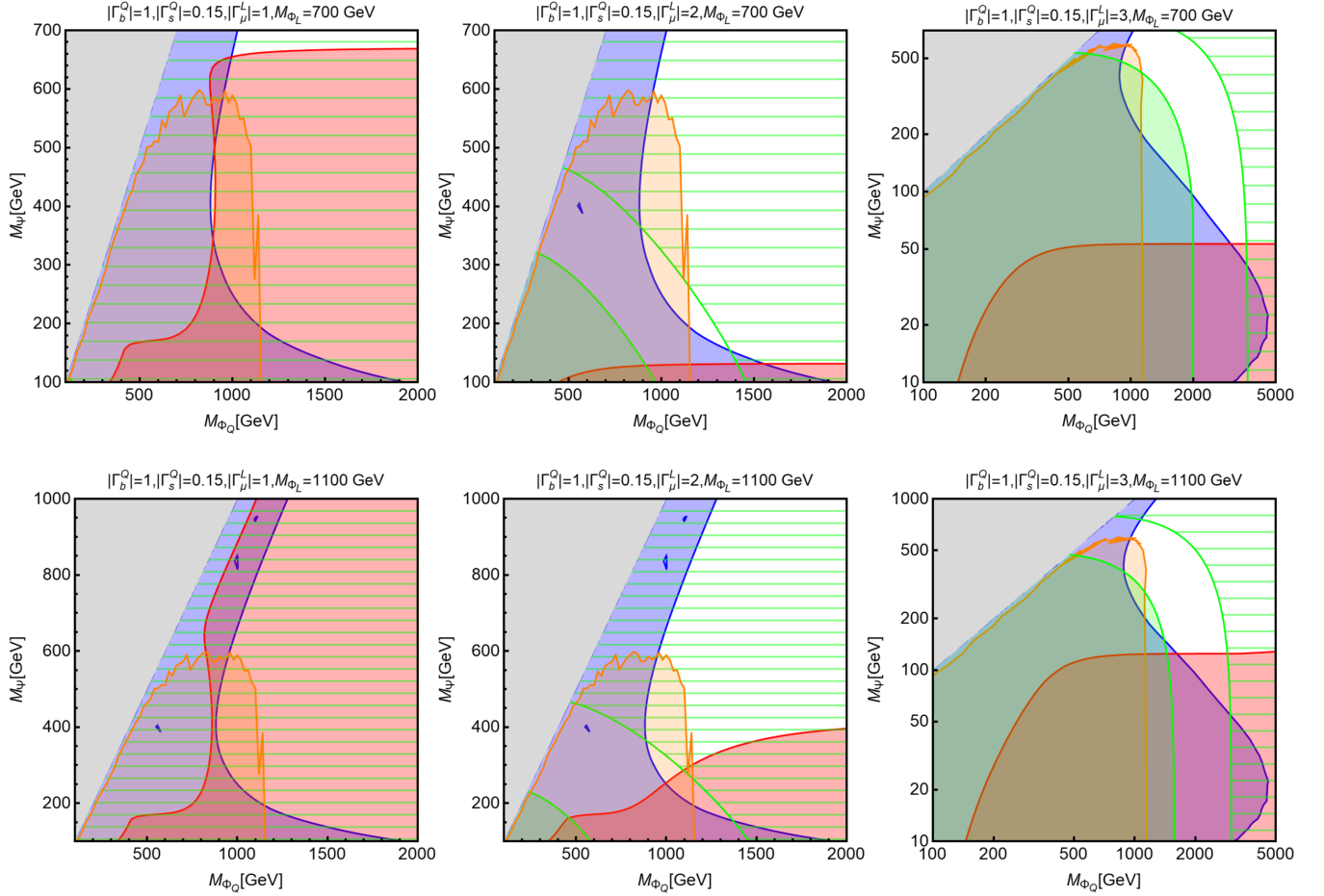This different outcome compared to the Dirac case is mostly due to the fact that, for Majorana DM, the effective
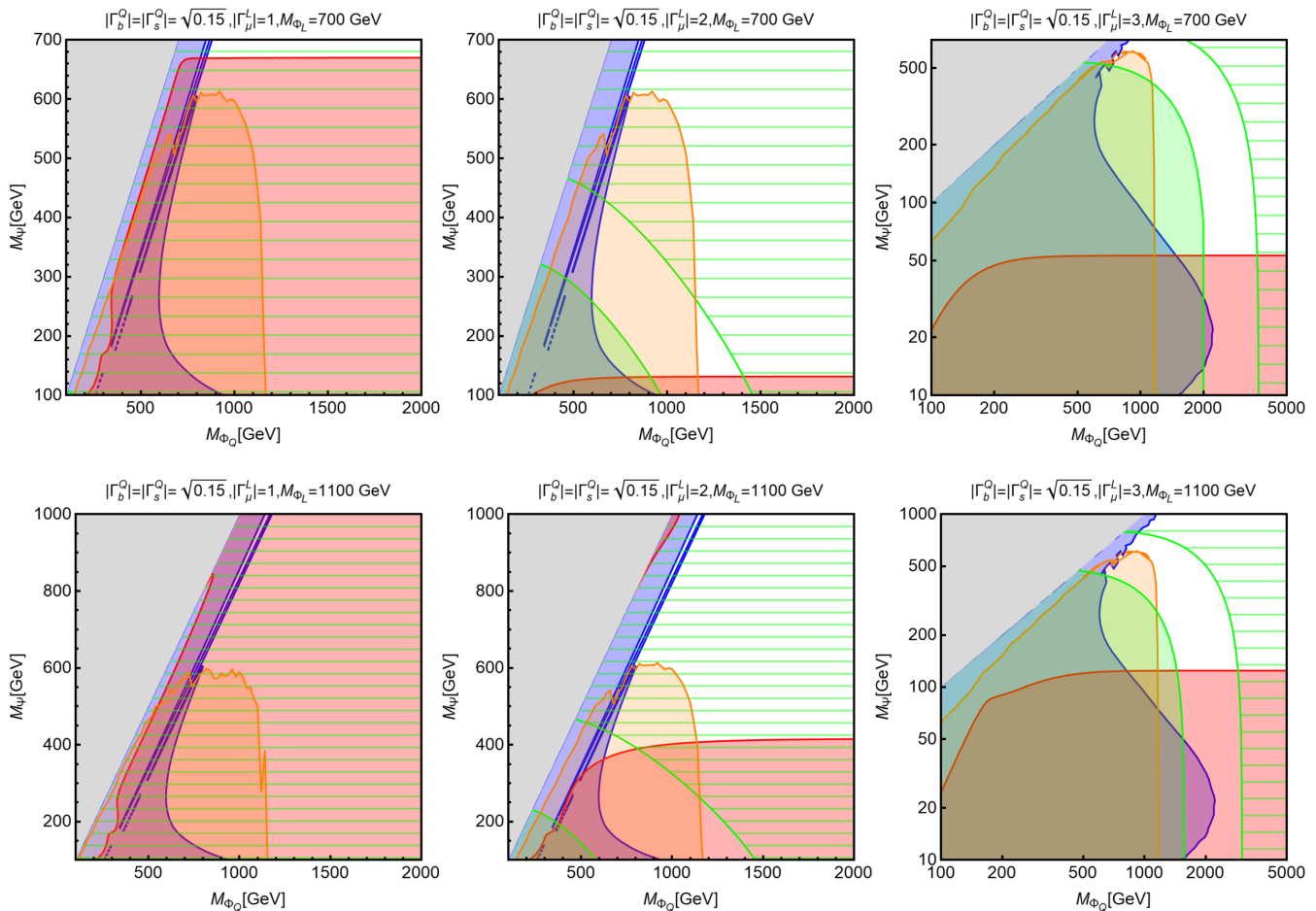
FIG. 6.   Summary of the constraints for the model $\mathcal{F}_{\mathrm{IA};0}$ with Majorana dark matter, with $|\Gamma_b^Q| = 1$, $|\Gamma_s^Q| = 0.15$, and the three assignments $|\Gamma_\mu^L| = 1, 2, 3$. The upper (lower) row corresponds to $M_{\Phi_L} = 700$ (1100) GeV. The color scheme is as defined in the caption of Fig. 5.

operators accounting for DM interactions with nucleons mediated by the Z boson and the photon identically vanish. As a consequence, the strength of the interactions between DM and nuclei is strongly reduced and, hence, DD bounds are significantly weaker. Furthermore, the annihilation cross section of Majorana DM is p-wave suppressed, and thus ID constraints are not present. Although this is a successful scenario according to our criteria, we remark again that, in order to have compatibility between the fit of the flavor anomaly and the other constraints, rather large values of the coupling to muons $|\Gamma_\mu^L|$ are required: $|\Gamma_\mu^L| \gtrsim 2$ for $M_{\Phi_L} \gtrsim 700$ GeV and $|\Gamma_\mu^L| \gtrsim 3$ for $M_{\Phi_L} \gtrsim 1100$ GeV.

C. $\mathcal{F}_{\mathrm{IB};-1/3}$, real-scalar doublet DM

We now turn to consider an example with scalar DM. In this case, DM is a (real) neutral state which is part of the scalar $SU(2)$ doublet Φ_Q, $(\mathbf{1}, \mathbf{2}, 1/2)$. The other NP fields Φ_L and Ψ transform under the SM gauge group, respectively, as $(\bar{\mathbf{3}}, \mathbf{2}, -1/6)$ and $(\mathbf{3}, \mathbf{1}, -1/3)$. The Lagrangian resembles that of the previously considered model:

$$\mathcal{L}_{\mathrm{int}} = \Gamma_i^Q \bar{Q}_i P_R \Psi \Phi_Q + \Gamma_i^L \bar{L}_i P_R \Psi \Phi_L + \mathrm{H.c.} \quad (44)$$

This is the simplest model, with our general classification, featuring the DM belonging to a $SU(2)$ doublet. As discussed in Sec. II, our minimality criteria only allow scalar DM to belong to an $SU(2)$ multiplet. Notice also that, as usual, the DM field Φ_Q and the other NP scalar Φ_L could couple with the Higgs field and among each other through operators of the types $|\Phi_Q|^2 |\Phi_L|^2$, $|H|^2 |\Phi_Q|^2$, and $|H|^2 |\Phi_L|^2$. As already pointed out, we are assuming in this work that these quartic couplings are so small that have a negligible impact on phenomenology. The only exception is given by the coupling providing a mass splitting between real and imaginary parts of the neutral component of Φ_Q, as discussed below. In fact, since the DM belongs to an $SU(2)$ doublet with nonzero hypercharge, it would feature as well tree-level interactions with the Z boson. In order to circumvent this possibility (which is already experimentally ruled out, see, e.g., Ref. [90]), we assume that, similarly to the so-called inert doublet model [125–128],

FIG. 7. Summary of the constraints for the model $\mathcal{F}_{\text{IA};0}$ with a Majorana dark matter, with $|\Gamma_b^Q| = |\Gamma_s^Q| = \sqrt{0.15}$, and the three assignments $|\Gamma_\mu^L| = 1, 2, 3$. The upper (lower) row corresponds to $M_{\Phi_L} = 700$ (1100) GeV. The color scheme is as defined in the caption of Fig. 5.

the neutral component of Φ_Q can be separated into a *CP*-even state, which we assume here to be the DM candidate, and a *CP*-odd state with a sufficient mass splitting [$\gtrsim \mathcal{O}(100)$ keV] to avoid DD constraints. This can be achieved through a quartic operator involving the SM Higgs of the form $(|\Phi_Q^\dagger H|^2 + \text{H.c.})$. Since a tiny coupling $\mathcal{O}(10^{-13})$ is enough to induce an $\mathcal{O}(100)$ keV mass splitting, we can safely assume that no other phenomenologically relevant effect follows from this (and other) Higgs-portal interactions.

The combined constraints on this model are shown, with the usual color coding, in Fig. 8 in the (M_Ψ, M_{Φ_Q}) plane (notice that what we label M_{Φ_Q} is just the DM mass). In contrast to the previous model, the strongest constraints come from flavor and LHC.[10] First, notice that we set

$M_{\Phi_L} = 1400$ GeV in order to evade bounds on Φ_L production and cascade decay ($pp \to \Phi_L\Phi_L \to \mu^+\mu^- + \Phi\Phi \to \mu^+\mu^- + qq' + \not\!\!E_T$) from the LHC searches in Refs. [76,77]. The dominant collider bound shown in the plots follows from the process $pp \to \Psi\Psi \to qq' + \Phi_Q\Phi_Q$, to which the CMS search of Ref. [72] is sensitive. On the other hand, the flavor anomalies are accounted for only for relatively light values of M_Ψ which fall in the region excluded by the CMS search,[11] with the exception of narrow tuned strips on the (M_Ψ, M_{Φ_Q}) plane corresponding to a very compressed spectrum, where jets would be too soft for a substantial number of events to be selected by the experimental cuts. We remark again that, even if it is not capable of accounting for the *B*-anomalies compatibly with all experimental constraints, the model $\mathcal{F}_{\text{IB};-1/3}$ is not strictly ruled out since LHC and DM constraints are evaded in large regions

---

[10]Here we have not considered bounds from disappearing tracks that would arguably have little sensitivity to the small production cross section and lifetime of the charged states of the doublet.

[11]This bound extends to substantially larger masses than in the previous case $\mathcal{F}_{\text{IA};0}$, as the produced particle here is a fermion; hence, its production cross section is about 1 order of magnitude larger than that of a scalar of the same mass.
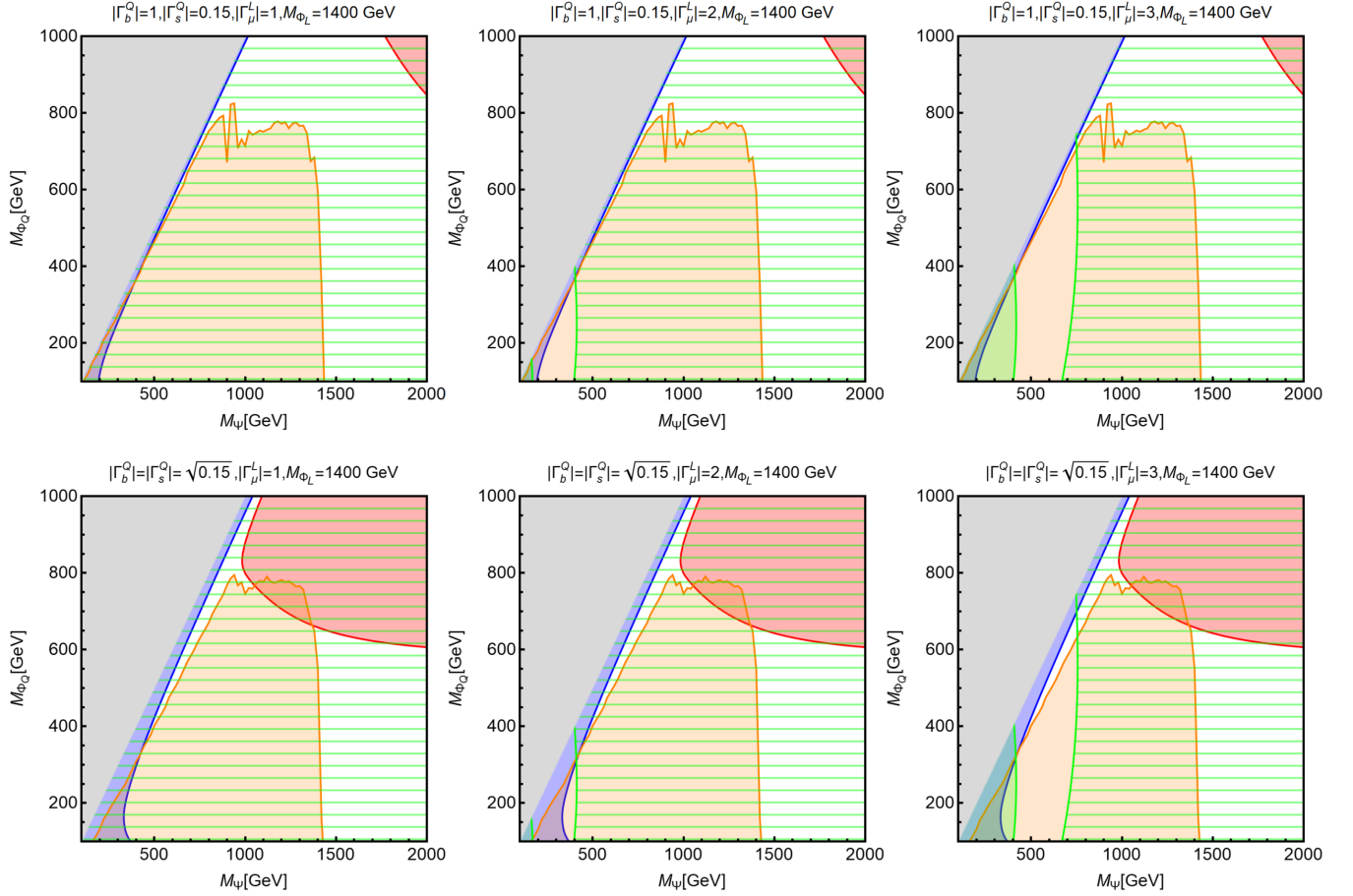
FIG. 8. Summary of the constraints for the model $\mathcal{F}_{\mathrm{IB};-1/3}$ with $|\Gamma_b^Q| = 1$, $|\Gamma_s^Q| = 0.15$, and the three assignments $|\Gamma_\mu^L| = 1, 2, 3$. The upper (lower) row correspond to configurations i) and ii) for the couplings of the NP fields. In all cases we have set $M_{\Phi_L} = 1400$ GeV. The color scheme is as defined in the caption of Fig. 5.

of the parameter space where the NP contributions to *B* observables do not exceed, in a statistically relevant way, the SM ones. Moving to DM phenomenology, we can see from Fig. 8 that direct detection constrains the model under consideration only poorly. This occurs because of the nature of DM: besides excluding tree-level interactions between DM pairs and the *Z* boson, the small mass splitting we assumed also sets to zero the $\Phi_Q^\dagger i \overleftrightarrow{\partial}_\mu \Phi_Q$ operator in the DD effective Lagrangian in Eq. (23). Finally, concerning DM relic density, we note that, similarly to what occurs in the case of the inert doublet model [125–128], very efficient annihilation processes into gauge bosons dominate DM production, as long as they are kinematically accessible. Thus, relatively large values of the DM mass ($\approx$500–600 GeV) outside the region fitting the *B* anomaly are required to have the correct relic density.

D. $\mathcal{S}_{\mathrm{IA}}$, complex-scalar singlet DM

This model is the counterpart of $\mathcal{F}_{\mathrm{IA};0}$ with scalar and fermion fields exchanging roles. It is then of primary interest due to the high degree of correlation among our observables. While a similar study of this scenario has been presented already in Ref. [30], our results are notably different, as discussed below.

The DM candidate belongs to the complex field Φ, which is a complete singlet under the SM gauge group. Since Φ also plays the role of the flavor mediator in the diagram of Fig. 1, it is not possible in this case to assume that it is a real scalar field, otherwise an additional "crossed" box diagram would exactly cancel the effect on $b \to s\ell\ell$, as can be seen from Eq. (9). The quantum numbers of the other two fields, Ψ_Q and Ψ_L, are, respectively, $(\mathbf{3}, \mathbf{2}, 1/6)$, $(\mathbf{1}, \mathbf{2}, -1/2)$, and the Lagrangian of the model reads

$$\mathcal{L}_{\mathrm{int}} = \Gamma_i^Q \bar{Q}_i P_R \Psi_Q \Phi + \Gamma_\mu^L \bar{L}_\mu P_R \Psi_L \Phi + \mathrm{H.c.} \quad (45)$$

Given our results for the $\mathcal{F}_{\mathrm{IA};0}$ model discussed in Sec. IV A, since the $\Phi^\dagger i \overleftrightarrow{\partial}_\mu \Phi$ operator behaves, in the nonrelativistic limit relevant for DM DD, in an analogous way as the Dirac DM operator $\bar{\Psi}\gamma^\mu\Psi$, we can expect this model to be completely ruled out by DM direct detection as
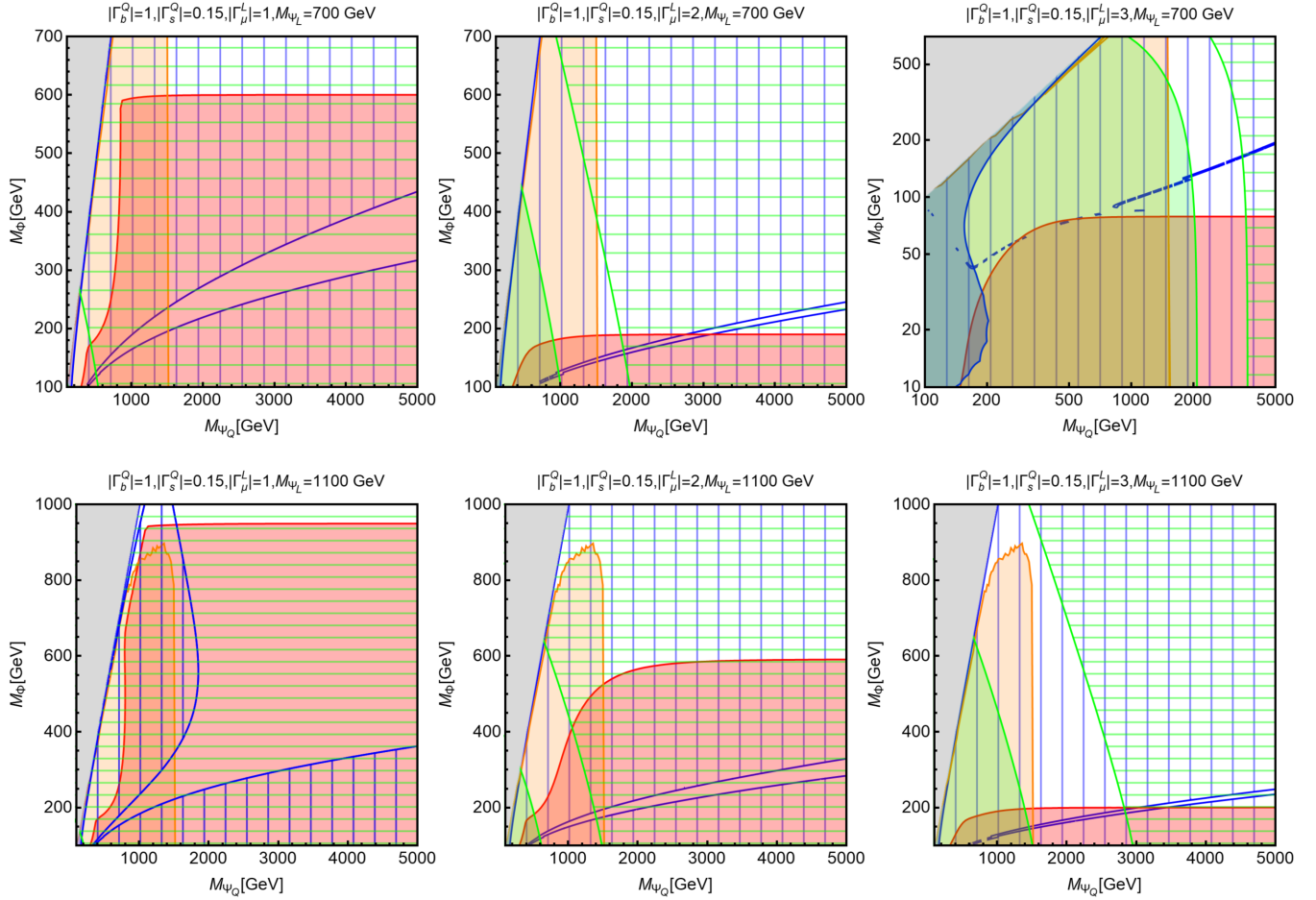
FIG. 9. Summary of the constraints for the model $\mathcal{S}_{\mathrm{IA}}$ with $|\Gamma_b^Q| = 1$, $|\Gamma_s^Q| = 0.15$, and the three assignments $|\Gamma_\mu^L| = 1, 2, 3$. The upper (lower) row corresponds to $M_{\Phi_L} = 700$ (1100) GeV. The color scheme is as in Fig. 5. In particular, the regions strictly excluded by DD are filled in blue, while the areas denoted by a vertical blue hatching are excluded only if the two components of the DM singlet are degenerate; see the text for details.

well. Furthermore, as we mentioned above, we cannot assume Φ to be a real scalar if we want the model to address the B-physics anomalies. To circumvent this problem, we can, however, assume that the two components of Φ (the real part and the imaginary part) have a small mass splitting $> \mathcal{O}(100)$ keV.[12] In this "nondegenerate" case the DM candidate would be a real scalar, the lightest of the two states. While this would ensure the needed suppression for the scattering cross section with nuclei, a small mass splitting would avoid the above-mentioned cancellation of $\delta C_\mu^{9,10}$ (the DM is the flavor mediator in this case) and maintain efficient DM annihilations. In fact, the annihilation cross section into SM fermions would be d-wave suppressed for real DM; hence, the correct relic density would follow from coannihilations of the two components of Φ.

The scenario with two degenerate states has been studied in Ref. [30].[13] Considering also the nondegenerate case will allow us to open a large viable region of the parameter space. Besides this important point, Ref. [30] differs from our study also from the fact that LHC data available at the time lead to less stringent bounds for couplings as in scenario (ii) compared to the limits in scenario (i). This is, however, not the case anymore, since the two scenarios are now no longer significantly different once the recasting of the CMS search of Ref. [72] is employed.

The combined constraints for this model are shown in Figs. 9 and 10. In these plots, the DD constraint for the degenerate case is shown as regions denoted by a vertical

---

[12]If DM is stabilized by a $\mathbf{Z}_2$ symmetry, this can be achieved for instance through an invariant term in the scalar potential of the form $\mu^2(\Phi^2 + \Phi^{*2})$ [35].

[13]A slightly more complicated variant of this model, featuring an additional scalar field, has been studied in Ref. [33]. Furthermore, adding to the model a scalar doublet mixing with the singlet through a coupling with the Higgs introduces interactions to right-handed fermions as well, allowing, in particular, a chirally enhanced contribution to $(g-2)_\mu$ and thus a natural explanation of the observed anomaly [50].
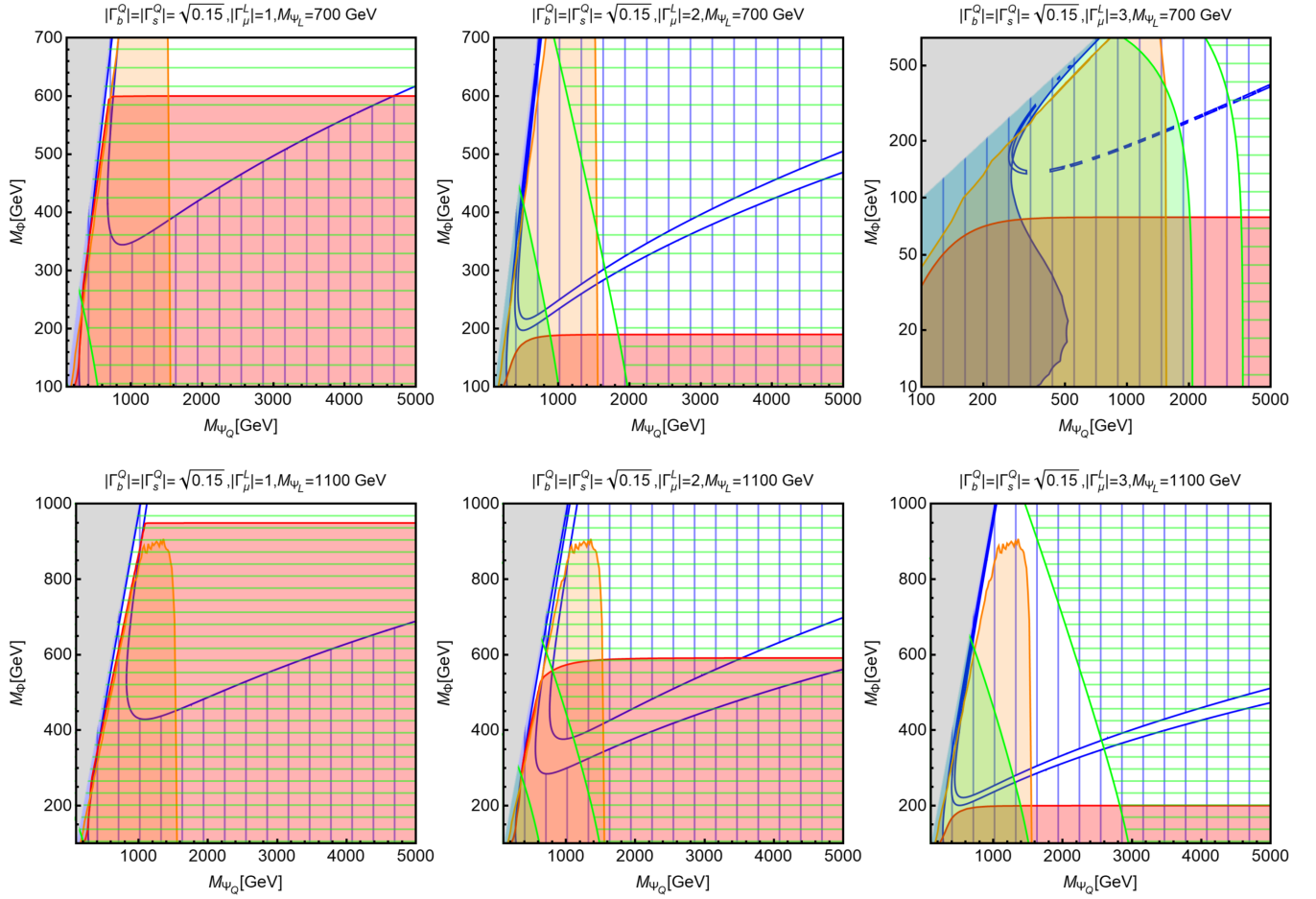
FIG. 10.   Summary of the constraints for the model $\mathcal{S}_{IA}$ with $|\Gamma_b^Q| = |\Gamma_s^Q| = \sqrt{0.15}$, and the three assignments $|\Gamma_\mu^L| = 1, 2, 3$. The upper (lower) row corresponds to $M_{\Phi_L} = 700$ (1100) GeV. The color scheme is as in Fig. 5. In particular, the regions strictly excluded by DD are filled in blue, while the areas denoted by a vertical blue hatching are excluded only if the two components of the DM singlet are degenerate; see the text for details.

blue hatching. As we can see, very efficient interactions mediated by the photon and the *Z*-boson penguins make the model subject to very strong constraints from XENON1T, such that only narrow tuned regions are compatible with a good fit of the flavor anomalies. On the other hand, assuming nondegenerate singlet states drastically reduces the exclusions from DD to the blue-filled areas, especially in the $M_{\Psi_Q} \simeq M_\Phi$ regime, where QCD operators for DD are relevant. In absence of strong bounds from direct detection, we see that the $\mathcal{S}_{IA}$ model can account for the *B* anomalies in wide regions of the parameter space. In addition, the correct DM relic density can be achieved for $\Gamma_\mu^L \gtrsim 2$ and $M_{\Psi_L} = 700$ GeV while for $M_{\Psi_L} = 1100$ GeV the coupling needs to be larger, $\Gamma_\mu^L \approx 3$. Thermal DM and a good fit of the flavor anomalies are thus simultaneously possible with DM masses approximately in the 50–200 GeV range.

E. $\mathcal{S}_{IIB}$, Dirac singlet DM

We now discuss another model with fermion singlet DM. The gauge quantum numbers of the NP fields are $(\mathbf{1}, \mathbf{1}, 0)$,

$(\bar{\mathbf{3}}, \mathbf{1}, -2/3)$, and $(\mathbf{3}, \mathbf{2}, 1/6)$ for Ψ_Q, Ψ_L, and Φ, respectively. The DM candidate is the Dirac field Ψ_Q, and the flavor mediator Φ is a complex scalar:

$$\mathcal{L}_{int} = \Gamma_i^Q \bar{Q}_i P_R \Psi_Q \Phi + \Gamma_i^L \bar{L}_i P_R \Psi_L \Phi + \text{H.c.} \quad (46)$$

This model is characterized by the fact that the DM field only couples to quarks and not to muons. It then allows for an interesting comparison with the $\mathcal{F}_{IA;0}$ model. Similarly to the latter scenario we will consider, respectively, here and in the next subsection, both cases of Dirac and Majorana DM.

The results of our analysis are shown in Fig. 11 and confirm the tendency, already observed for $\mathcal{F}_{IA;0}$, of models with Dirac DM of being already experimentally excluded. Compared to the $\mathcal{F}_{IA;0}$ scenario we notice some differences though. First of all, the relic density constraint is much stronger and, moreover, is not sensitive to the value of the Γ_μ^L coupling. In fact, all DM phenomenology does not depend on this latter parameter (neither on M_{Ψ_L}), as it
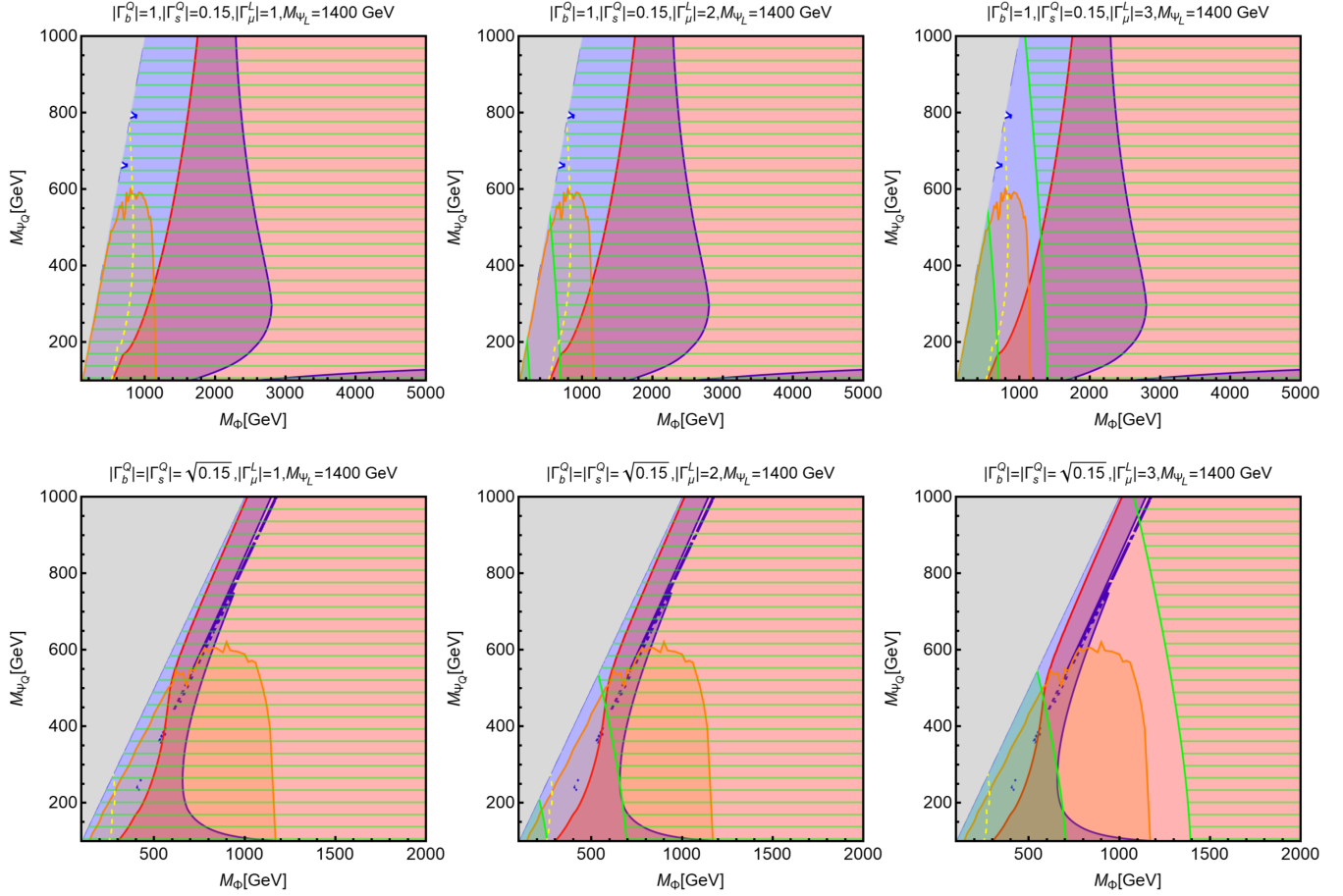
FIG. 11. Summary of the constraints for the model $\mathcal{S}_{\text{IIB}}$ with Dirac DM. The upper row refers to the assignments $|\Gamma_s^Q| = 1$, $|\Gamma_s^Q| = 0.15$, while the lower row corresponds instead to $|\Gamma_b^Q| = |\Gamma_s^Q| = \sqrt{0.15}$. In all cases we have set $M_{\Psi_L} = 1400$ GeV and $|\Gamma_\mu^L| = 1$, 2, 3. The color scheme is as defined in the caption of Fig. 5.

can be seen by comparing the three columns of plots of Fig. 11. This is due to the fact that the DM field is now only coupled with the field Φ and left-handed quarks. DM observables hence depend only on the $\Gamma_{s,b}^Q$ couplings which are fixed by the fit of flavor observables. Furthermore, as it is the coupling with muons absent, the DM annihilation cross section is more suppressed than in the $\mathcal{F}_{\text{IA};0}$ model, especially for configuration (ii) of the couplings. Looking instead at direct detection, while being still the most challenging constraint for assignment (i) of the couplings, its impact is strongly reduced, relative to the requirement of the viable relic density, for assignment (ii). This is because the most relevant contribution to the SI cross section here comes from loop diagrams involving the Z bosons, whose effect is enhanced by the mass of the top quark. Since the coupling of the DM field with the top is reduced, once moving from assignment (i) to (ii), the DM scattering rate is consequently reduced. We have not observed such an outcome in the model $\mathcal{F}_{\text{IA};0}$ since a comparable or even larger contribution to the DM scattering rate on nucleons

was coming from interactions with the photon, controlled by the Γ_μ^L coupling.

As mentioned above, in the $\mathcal{S}_{\text{IIB}}$ models, all the phenomenological constraints are independent on the M_{Ψ_L} and Γ_μ^L parameters [as long as Ψ_L is heavy enough to evade searches for cascade decays as in Eq. (14)] with the exception of the region favored by B physics. Moreover, we have found that the latter changes only marginally for different values of M_{Ψ_L}. Hence, we have set for all plots $M_{\Psi_L} = 1400$ GeV, a value that allows us to evade the constraint on $pp \to \Psi_L \Psi_L \to \mu^+ \mu^- + \Phi\Phi \to \mu^+ \mu^- + qq' + \not{E}_T$ of the searches in Refs. [76,77]. Figure 11 shows that, mainly due to the combined effect of relic density and DD constraints, this model is ruled out way beyond the region favored by the flavor anomalies. One could possibly overcome this problem by assuming a nonstandard cosmological history of the early Universe; see, e.g., [112,113,129–131], such that the DM abundance is diluted to the extent that the region compatible with the flavor anomalies in the last plot of Fig. 11 becomes partly viable.
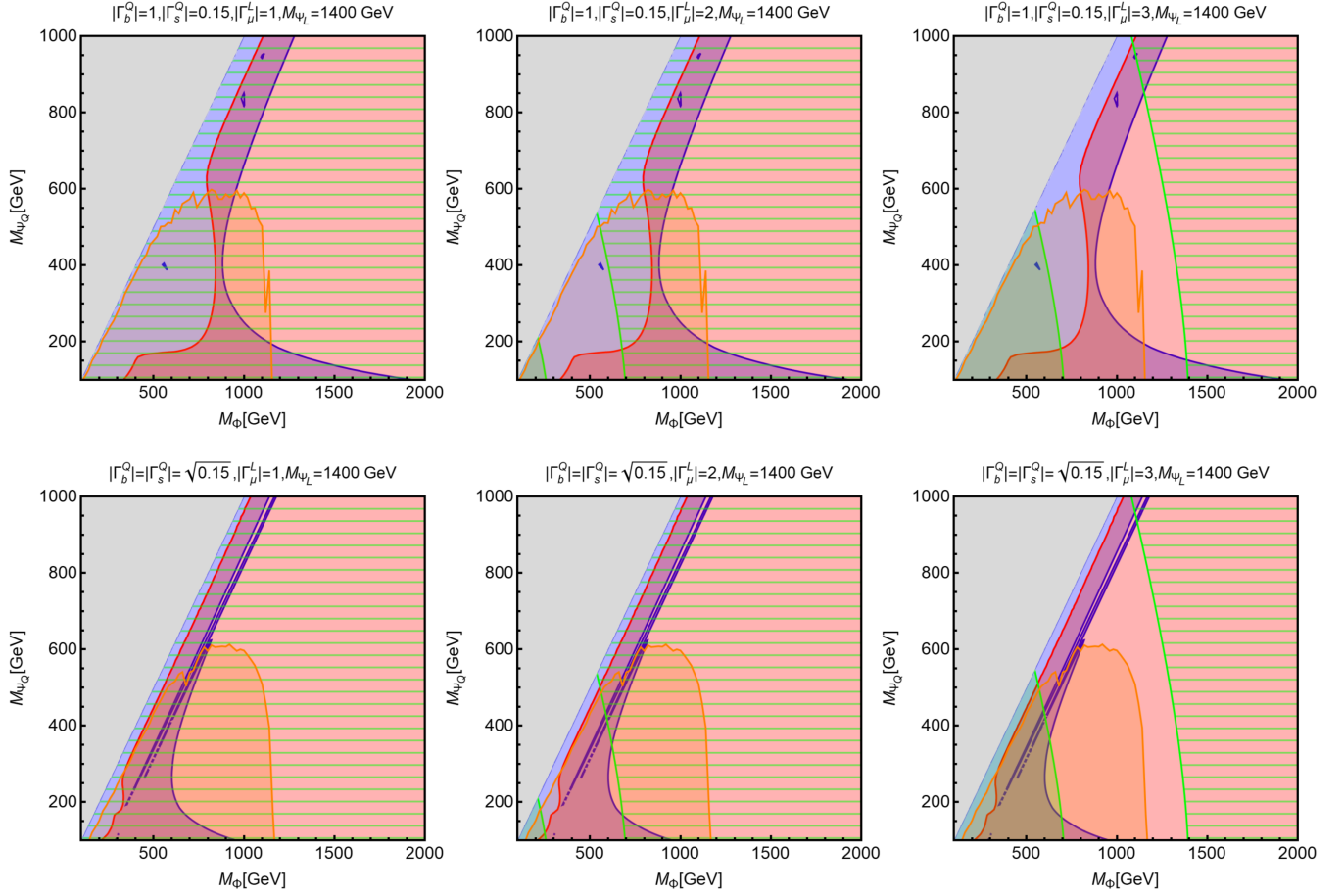
FIG. 12.   Same as Fig. 11 but for $\mathcal{S}_{\mathrm{IIB}}$ with Majorana DM.

F. $\mathcal{S}_{\mathrm{IIB}}$, Majorana singlet DM

Here, we consider a variant of the previous model featuring Majorana rather than Dirac DM. As shown in Fig. 12, this time moving from Dirac to Majorana, DM does not open new viable regions of the parameter space. The Majorana nature of the DM particle eliminates the Z-penguin contribution to the scattering with nuclei discussed in the previous subsection. This noticeably relaxes the DD constraints for the case of large couplings to the top as in our scenario (*i*), shown in the first line of Fig. 12. However, irreducible QCD contributions to DD still impact the parameter space even for Majorana DM. Furthermore, the region compatible with the flavor constraints typically corresponds to an overabundance of DM. In the Majorana case, the DM annihilation cross section is even more suppressed, because of velocity dependence, with respect to the case of Dirac DM. As a result, this model is still not viable unless a nonstandard cosmology provides additional DM dilution. As already pointed out, this outcome follows from the fact that the DM is coupled only with one NP state. This is the main difference with, e.g., model $\mathcal{F}_{\mathrm{IA;0}}$ that, as we showed in Sec. IV B, easily fulfills all constraints in the case of Majorana DM.

G. $\mathcal{S}_{\mathrm{IIIA;-1/2}}$, Majorana triplet DM

To conclude our overview of scenarios with distinct phenomenology, we illustrate two models with DM belonging to a $SU(2)_L$ triplet. In fact notice that, for all models in Tables II and III featuring a complete singlet, gauge invariance allows us to substitute to the singlet an $SU(2)_L$ triplet with zero hypercharge. As we will see below, the consequent change in the phenomenology of our models is dramatic.

We start with the model $\mathcal{S}_{\mathrm{IIIA;-1/2}}$, whose DM candidate is part of the fermion triplet Ψ_L, $(\mathbf{1}, \mathbf{3}, 0)$. The field Ψ_Q also transforms as an $SU(2)_L$ triplet, as well as a color triplet: $(\mathbf{3}, \mathbf{3}, 2/3)$. The mediator is a complex-scalar doublet $(\mathbf{1}, \mathbf{2}, -1/2)$. The Lagrangian reads

$$\mathcal{L}_{\mathrm{int}} = \Gamma_i^Q \bar{Q}_i P_R (\tau^a \Psi_Q^a) \Phi + \Gamma_\mu^L \bar{L}_\mu P_R (\tau^a \Psi_L^a) \Phi + \mathrm{H.c.}, \quad (47)$$

As mentioned above, the DM candidate is the neutral component of the Majorana field Ψ_L.

The combined constraints on this model are shown in Fig. 13. We consider again the single assignment $M_{\Psi_Q} = 1400$ GeV, as our usual benchmark values 700, 1100 GeV are mostly excluded by recasting the LHC
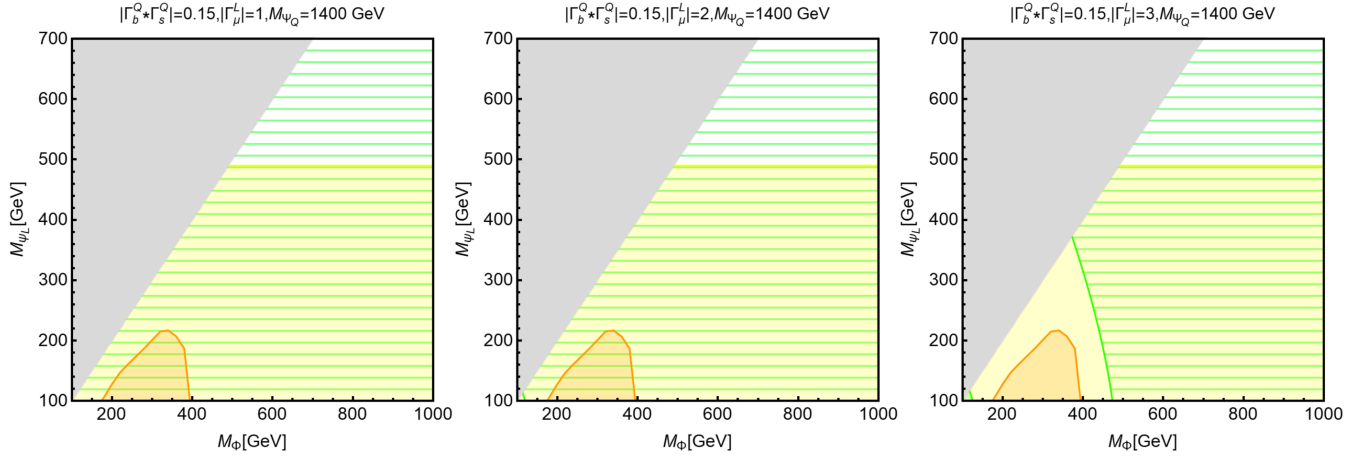
FIG. 13. Summary of the constraints for the model $\mathcal{S}_{\mathrm{IIIA};-1/2}$ with triplet Majorana DM. We have considered the values 1,2,3 for the $|\Gamma_\mu^Q|$ coupling. Contrary to the other models, DM constraints do not depend on the individual values of the Γ_s^Q and Γ_b^Q couplings; hence, they have not made the usual distinction between the configurations (*i*) and (*ii*). The color scheme is as defined in Fig. 5. In addition, the yellow region is excluded by LHC searches of disappearing tracks; see the text for details.

searches in Refs. [76,77] in terms of the process $pp \to \Psi_Q \Psi_Q \to qq' + \Phi\Phi \to qq' + \mu^+\mu^- + \not{E}_T$.

The $\mathcal{S}_{\mathrm{IIIA};-1/2}$ model features the weakest correlation among flavor/LHC and DM observables. As we can see from the Lagrangian, the DM is coupled only with the color singlet Φ. Being, in addition, a Majorana fermion, the only contribution to SI interactions comes from loop diagrams involving the charged components of the DM multiplet Ψ_L as well as the W, Z bosons [60,122]. These kinds of interactions lead to cross sections still below current experimental sensitivity [132,133]. For this reason no DD exclusion region appears in Fig. 13. For what concerns the relic density, belonging the DM candidate to a triplet, it features a very efficient and possibly Sommerfeld-enhanced annihilation cross section into gauge boson pairs (cf., e.g., the third diagram in Fig. 2) such that the CMB bound $\Omega_{\mathrm{DM}}h^2 \simeq 0.12$ is saturated only for DM masses of the order of 3 TeV, far from the region compatible with the fit of flavor observables. In the regime shown in the plots, the DM is always underabundant (unless some nonthermal production mechanism is assumed), irrespective of the values of the masses and couplings of the NP fields and, hence, no relic density exclusion appears. From Fig. 13, we can also see that the region excluded by LHC searches for events featuring missing energy (in this case $pp \to \Phi\Phi \to \mu^+\mu^- + \not{E}_T$ [73]) is not very pronounced. However, compared to the previous models, these plots feature a new type of excluded region, filled in yellow. This bound corresponds to the negative results from LHC searches [80,81] for the disappearing charged tracks that, in the model under consideration, would be associated to the pair production of the electrically charged components of the electroweak multiplet the DM belongs to; see the related discussion in Sec. III B. In the minimal setup considered in this work, the different states composing the DM multiplet have

loop-suppressed $\mathcal{O}(100)$ MeV mass splitting determined by electroweak gauge interactions. As a consequence, the charged DM partner is long lived and decays into final state particles which are too soft to be detected or would be, hence leading to disappearing-track events rather than prompt jets or leptons and missing energy events. For the $\mathcal{S}_{\mathrm{IIIA};-1/2}$ model we can directly apply the disappearing-track bound obtained for the case of a supersymmetric Wino [81] which translates into a limit of the triplet mass $M_{\Psi_L} \geq 490$ GeV. As we can see, this latter bound completely covers the region fitting the flavor anomalies.

H. $\mathcal{F}_{\mathrm{IIIA};-1/2}$, real-scalar triplet DM

The last model we consider is analogous to the previous one with the role of fermion and scalar fields reversed. It is described by the following Lagrangian:

$$\mathcal{L}_{\mathrm{int}} = \Gamma_i^Q \bar{Q}_i P_R (\tau^a \Phi_Q^a) \Psi + \Gamma_\mu \bar{L}_\mu P_R (\tau^a \Phi_L^a) \Psi + \mathrm{H.c.}, \quad (48)$$

and the $SU(3)$, $SU(2)_L$, and $U(1)_Y$ quantum numbers of the NP fields are $(\mathbf{3}, \mathbf{3}, 2/3)$, $(\mathbf{1}, \mathbf{3}, 0)$, and $(\mathbf{1}, \mathbf{2}, -1/2)$ for Φ_Q, Φ_L, and Ψ, respectively. The DM candidate is the neutral component of the scalar triplet Φ_L, and the mediator is the fermion doublet Ψ.

The effect of the combined constraints on the $\mathcal{F}_{\mathrm{IIIA};-1/2}$ model is shown in Fig. 14. For analogous reasons to those illustrated in the previous subsection, also in the case of scalar triplet DM, we notice the absence of bounds coming from DM direct detection and relic density. Detailed studies of the DM phenomenology of real scalar triplets have been conducted, e.g., in Refs. [134,135]. A notable difference with respect to the previous model $\mathcal{S}_{\mathrm{IIIA};-1/2}$ emerges, on the contrary, for what concerns LHC bounds. Indeed, the bounds from missing energy events (specifically on
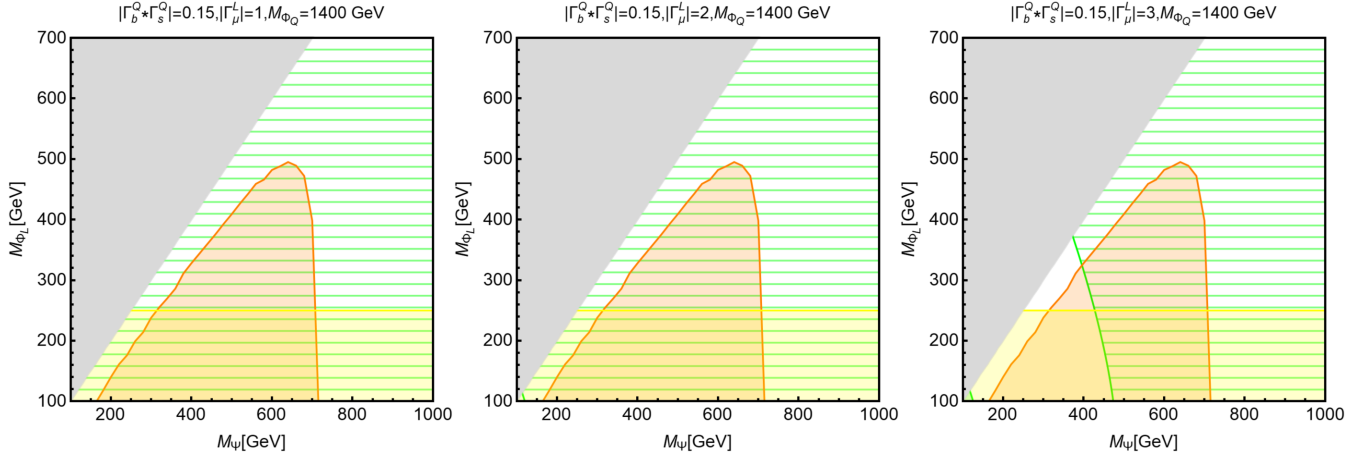
FIG. 14. Summary of the constraints for the $\mathcal{F}_{\text{IIIA};-1/2}$ model with scalar triplet DM. Similarly to $\mathcal{S}_{\text{IIIA};-1/2}$, the model is constrained only by flavor and LHC and the constraints do not depend on the individual values of Γ_s^Q, Γ_b^Q. The color scheme is as defined in Fig. 5. The yellow region is excluded by LHC searches of disappearing tracks.

$pp \to \Psi\Psi \to \mu^+\mu^- + \not{E}_T$ [73]) impact a larger (orange) region of the parameter space, compared to the analogous model with fermionic DM. This is again due to the fact that the Drell-Yan production cross section of the fermion pair Ψ is substantially larger than the one of a scalar pair with the same mass and the same quantum numbers under the SM gauge group. On the contrary, the bound from disappearing tracks (here we show the limit as recasted for the case of a scalar triplet in Ref. [134]) is weaker for scalar DM, again due to the different production cross section. As a consequence, we notice the presence of (narrow) regions of the parameter space compatible with the flavor anomalies, provided that $|\Gamma_\mu^L| \gtrsim 3$. We expect that these unconstrained regions can be tested employing future LHC data by a combination of searches for disappearing tracks and searches for events with soft leptons and missing energy like those in Refs. [74,75].

V. SUMMARY AND CONCLUSIONS

In this work, we have presented a systematic study of minimal scenarios providing a viable fit of the observed anomalies in semileptonic *B*-meson decays and simultaneously solving the DM puzzle thanks to a particle candidate that can achieve, through the thermal freeze-out mechanism, a relic density compatible with the experimental determination from CMB anisotropies. In this minimal setup, the SM spectrum is extended by three new states, either two scalars and a fermion, or two fermions and a scalar, coupled, according to gauge invariance, with left-handed muons and quarks of the second and third generation. All these new fields, including the DM candidate, are present in the loop diagrams associated to the NP contributions to the rates of *B*-meson decays, as shown in Fig. 1. These kinds of models, hence, feature an interesting connection between flavor and DM physics. To our knowledge, the present work shows for

the first time a complete classification of the possible models of this kind which can be elaborated, depending on the quantum numbers of the new fields. The details of the considered setup are given in Sec. II and the outcome of such a classification is summarized in Tables II and III. In Sec. IV, we have studied, in detail, a selection of these models encompassing a large variety of scenarios. Among the models we chose, four possible natures for the DM candidate (namely, real scalar DM, complex-scalar DM, and Dirac and Majorana fermionic DM) are represented. Furthermore, our selection includes examples with the DM field being a singlet of $SU(2)_L$, as well as cases of DM belonging to an $SU(2)_L$ doublet or triplet. Following the strategy described in Sec. III, for each model we have performed a fit to the *B*-physics anomalies and used the results to define benchmark assignments for the couplings of the new particles with quarks as well as the mass of one of the (non-DM) NP fields. We have then studied, in terms of the remaining parameters, a broad range of constraints: bounds from searches for the new states at the LHC, DM relic density, DM direct detection and, when appropriate, DM indirect detection.

The results of this analysis have been presented in detail in Sec. IV, and the general lessons that we can extract from it can be summarized as follows.

(i) A good fit to the flavor anomalies is possible if the product of the couplings of the NP fields to bottom and strange quarks is moderate $\Gamma^Q \sim 0.15$ (larger values would be in conflict with constraints from B_s mixing) and consequently the coupling to muons must be rather large $\Gamma_\mu^L \gtrsim 2$ (to fit the anomalies at the 2σ level, cf. Sec. III A). This has important consequences for DM phenomenology: if DM belongs to one of the two fields coupled to muons, annihilations into muons are very efficient in depleting the DM abundance to (or below) the

observed value. Moreover, electroweak penguin diagrams like the one depicted in Fig. 4 can give a large contribution to the DM-nucleon scattering cross section relevant for DM direct detection.

(ii) As a consequence, in the cases with DM coupling to muons, especially if it belongs to the field (Φ or Ψ) that acts as "flavor messengers" in Fig. 1, we observe a high degree of correlation among our observables, namely, the couplings of the NP fields to SM fermions simultaneously control DM, flavor, and collider observables (this is the case for instance of models $\mathcal{F}_{\mathrm{IA};0}$ and $\mathcal{S}_{\mathrm{IA}}$ featuring singlet DM). Furthermore, the relic density constraints can be easily satisfied in the region of the parameter space that fits the flavor anomalies.

(iii) However, strong constraints from DM direct detection would substantially rule out these scenarios, unless DM is a Majorana fermion or a real scalar (cases for which the most relevant DM-nucleon operator vanishes) or it is a complex scalar with a mass splitting $> \mathcal{O}(100)$ keV between its two components (making the scattering inelastic). In fact, model $\mathcal{F}_{\mathrm{IA};0}$ with Dirac DM is completely excluded (cf. Fig. 5) while it is among the most favorable scenarios from an experimental perspective if DM is Majorana; see Figs. 6 and 7. Similarly, $\mathcal{S}_{\mathrm{IA}}$ is a viable option and fits well both DM and the flavor anomalies only if the above-mentioned mass splitting is assumed; cf. Figs. 9 and 10. Interestingly, the viable regions of the parameter space of these models are already partially constrained by LHC searches for jets/muons and missing energy and by direct detection; hence, they have good prospects of being tested by next generation detectors like XENONnT [136] and future runs of the LHC [137].

(iv) For models where DM is still a singlet but couples only to quarks (such as in the example $\mathcal{S}_{\mathrm{IIB}}$), DM annihilation is typically not efficient enough and the fit of the flavor anomalies points toward regions of the parameter space where DM is overproduced. These cases are then typically excluded by the relic density constraint independent of whether DM is a Dirac or a Majorana field, cf. Figs. 11 and 12, but they could be possibly viable within modified cosmological histories of the early Universe providing additional DM dilution.

(v) Our analysis also shows that a combined fit of DM and flavor anomalies favors scenarios where DM is a singlet of the SM gauge group. If DM is instead part of an $SU(2)_L$ multiplet the correlation between relic density and flavor observables is lost, as DM annihilation mainly proceeds through gauge interactions, thus independently on the couplings with quarks and leptons. Furthermore, one should rely on a nonthermal DM production mechanism since, in

the regions of parameter space where a viable fit of the B anomalies is achieved, the DM is always underabundant in light of its very efficient annihilations into gauge bosons; see models $\mathcal{F}_{\mathrm{IB};-1/3}$, $\mathcal{S}_{\mathrm{IIIA}}$, and $\mathcal{F}_{\mathrm{IIIA}}$. The main challenge to these kinds of models comes from LHC searches. In particular, in case of DM belonging to an $SU(2)_L$ triplet, the interesting signature of disappearing charged tracks excludes or drastically restricts the regions of the parameter space compatible with the flavor physics anomalies; see Figs. 13 and 14.

As mentioned in the Introduction, the present exercise did not aim at proposing "realistic" BSM scenarios, but rather at highlighting the minimal ingredients that a more fundamental theory may need to include if the new physics (possibly) behind the B-physics anomalies is indeed related to the DM sector. The above analysis studied the role and the phenomenological consequences of such minimal building blocks. These scenarios could be easily extended to include more particles and interactions. In particular, additional vectorlike fermions or scalars, mixing through a SM Higgs vacuum expectation value with the fields considered here, would also induce operators involving right currents that may provide an even better fit to the $b \to s\ell\ell$ data. Similarly, this would introduce couplings to right-handed muons that can realize chirally enhanced contributions to the muon $g-2$ and thus a natural fit of the observed anomaly; see, e.g., [29,70,71,138,139]. Moreover, a more realistic flavor structure of the couplings (rather than our *ad hoc* assignment) could be considered, possibly following from some flavor symmetry or other models explaining the observed hierarchies of fermion masses and mixing. Within frameworks of such kinds, one could find correlations between our observables and flavor processes in other sectors (e.g., $s-d$ transitions), and thus additional constraints and handles to test the scenarios we considered.

[1] G. Bertone and D. Hooper, History of dark matter, Rev. Mod. Phys. **90**, 045002 (2018).

[2] R. Aaij *et al.* (LHCb Collaboration), Search for Lepton-Universality Violation in $B^+ \to K^+\ell^+\ell^-$ Decays, Phys. Rev. Lett. **122**, 191801 (2019).

[3] R. Aaij *et al.* (LHCb Collaboration), Test of lepton universality with $B^0 \to K^{*0}\ell^+\ell^-$ decays, J. High Energy Phys. 08 (2017) 055.

[4] A. Abdesselam *et al.* (Belle Collaboration), Test of Lepton Flavor Universality in $B \to K^*\ell^+\ell^-$ Decays at Belle, Phys. Rev. Lett. **126**, 161801 (2021).

[5] R. Aaij *et al.* (LHCb Collaboration), Angular analysis of the $B^0 \to K^{*0}\mu^+\mu^-$ decay using 3 fb^{-1} of integrated luminosity, J. High Energy Phys. 02 (2016) 104.

[6] R. Aaij *et al.* (LHCb Collaboration), Angular analysis of the B^0 to $K^{*0}e^+e^-$ decay in the low-q^2 region, J. High Energy Phys. 04 (2015) 064.

[7] R. Aaij *et al.* (LHCb Collaboration), Measurements of the S-wave fraction in $B^0 \to K^+\pi^-\mu^+\mu^-$ decays and the $B^0 \to K^*(892)^0\mu^+\mu^-$ differential branching fraction, J. High Energy Phys. 11 (2016) 047; Erratum, J. High Energy Phys. 04 (2017) 142.

[8] S. Wehle *et al.* (Belle Collaboration), Lepton-Flavor-Dependent Angular Analysis of $B \to K^*\ell^+\ell^-$, Phys. Rev. Lett. **118**, 111801 (2017).

[9] M. Aaboud *et al.* (ATLAS Collaboration), Angular analysis of $B_d^0 \to K^*\mu^+\mu^-$ decays in pp collisions at $\sqrt{s} =$ 8 TeV with the ATLAS detector, J. High Energy Phys. 10 (2018) 047.

[10] V. Khachatryan *et al.* (CMS Collaboration), Angular analysis of the decay $B^0 \to K^{*0}\mu^+\mu^-$ from pp collisions at $\sqrt{s} =$ 8 TeV, Phys. Lett. B **753**, 424 (2016).

[11] A. M. Sirunyan *et al.* (CMS Collaboration), Measurement of angular parameters from the decay $B^0 \to K^{*0}\mu^+\mu^-$ in proton-proton collisions at $\sqrt{s} =$ 8 TeV, Phys. Lett. B **781**, 517 (2018).

[12] R. Aaij *et al.* (LHCb Collaboration), Measurement of *CP*-Averaged Observables in the $B^0 \to K^{*0}\mu^+\mu^-$ Decay, Phys. Rev. Lett. **125**, 011802 (2020).

[13] R. Aaij *et al.* (LHCb Collaboration), Angular Analysis of the $B^+ \to K^{*+}\mu^+\mu^-$ Decay, Phys. Rev. Lett. **126**, 161802 (2021).

[14] R. Aaij *et al.* (LHCb Collaboration), Angular analysis and differential branching fraction of the decay $B_s^0 \to \phi\mu^+\mu^-$, J. High Energy Phys. 09 (2015) 179.

[15] S. Descotes-Genon, J. Matias, and J. Virto, Understanding the $B \to K^*\mu^+\mu^-$ Anomaly, Phys. Rev. D **88**, 074002 (2013).

[16] W. Altmannshofer and D. M. Straub, New physics in $B \to K^*\mu\mu$?, Eur. Phys. J. C **73**, 2646 (2013).

[17] D. Ghosh, M. Nardecchia, and S. A. Renner, Hint of lepton flavour non-universality in *B* meson decays, J. High Energy Phys. 12 (2014) 131.

[18] G. D'Amico, M. Nardecchia, P. Panci, F. Sannino, A. Strumia, R. Torre, and A. Urbano, Flavour anomalies after the R_{K^*} measurement, J. High Energy Phys. 09 (2017) 010.

[19] M. Ciuchini, A. M. Coutinho, M. Fedele, E. Franco, A. Paul, L. Silvestrini, and M. Valli, New physics in $b \to s\ell^+\ell^-$ confronts new data on lepton universality, Eur. Phys. J. C **79**, 719 (2019).

[20] M. Algueró, B. Capdevila, A. Crivellin, S. Descotes-Genon, P. Masjuan, J. Matias, M. Novoa Brunet, and J. Virto, Emerging patterns of New Physics with and without Lepton Flavour Universal contributions, Eur. Phys. J. C **79**, 714 (2019).

[21] A. K. Alok, A. Dighe, S. Gangal, and D. Kumar, Continuing search for new physics in $b \to s\mu\mu$ decays: Two operators at a time, J. High Energy Phys. 06 (2019) 089.

[22] A. Datta, J. Kumar, and D. London, The *B* anomalies and new physics in $b \to se^+e^-$, Phys. Lett. B **797**, 134858 (2019).

[23] J. Aebischer, W. Altmannshofer, D. Guadagnoli, M. Reboud, P. Stangl, and D. M. Straub, *B*-decay discrepancies after Moriond 2019, Eur. Phys. J. C **80**, 252 (2020).

[24] K. Kowalska, D. Kumar, and E. M. Sessolo, Implications for new physics in $b \to s\mu\mu$ transitions after recent measurements by Belle and LHCb, Eur. Phys. J. C **79**, 840 (2019).

[25] M. Ciuchini, M. Fedele, E. Franco, A. Paul, L. Silvestrini, and M. Valli, Lessons from the $B^{0,+} \to K^{*0,+}\mu^+\mu^-$ angular analyses, Phys. Rev. D **103**, 015030 (2021).

[26] T. Hurth, F. Mahmoudi, and S. Neshatpour, Model independent analysis of the angular observables in $B^0 \to K^{*0}\mu^+\mu^-$ and $B^+ \to K^{*+}\mu^+\mu^-$, Phys. Rev. D **103**, 095020 (2021).

[27] B. Gripaios, M. Nardecchia, and S. Renner, Linear flavour violation and anomalies in *B* physics, J. High Energy Phys. 06 (2016) 083.

[28] P. Arnan, L. Hofer, F. Mescia, and A. Crivellin, Loop effects of heavy new scalars and fermions in $b \to s\mu^+\mu^-$, J. High Energy Phys. 04 (2017) 043.

[29] P. Arnan, A. Crivellin, M. Fedele, and F. Mescia, Generic loop effects of new scalars and fermions in $b \to s\ell^+\ell^-$ and a vector-like 4th generation, J. High Energy Phys. 06 (2019) 118.

[30] J. Kawamura, S. Okawa, and Y. Omura, Interplay between the $b \to s\ell\ell$ anomalies and dark matter physics, Phys. Rev. D **96**, 075041 (2017).

[31] J. M. Cline and J. M. Cornell, $R(K^{(*)})$ from dark matter exchange, Phys. Lett. B **782**, 232 (2018).

[32] B. Barman, D. Borah, L. Mukherjee, and S. Nandi, Correlating the anomalous results in $b \to s$ decays with inert Higgs doublet dark matter and muon $(g - 2)$, Phys. Rev. D **100**, 115010 (2019).

[33] B. Grinstein, S. Pokorski, and G. G. Ross, Lepton non-universality in *B* decays and fermion mass structure, J. High Energy Phys. 12 (2018) 079.

[34] D. G. Cerdeño, A. Cheek, P. Martín-Ramiro, and J. M. Moreno, *B* anomalies and dark matter: A complex connection, Eur. Phys. J. C **79**, 517 (2019).

[35] D. Huang, A. P. Morais, and R. Santos, Anomalies in *B*-meson decays and the muon $g - 2$ from dark loops, Phys. Rev. D **102**, 075009 (2020).

[36] D. Aristizabal Sierra, F. Staub, and A. Vicente, Shedding light on the $b \to s$ anomalies with a dark sector, Phys. Rev. D **92**, 015001 (2015).

[37] G. Bélanger, C. Delaunay, and S. Westhoff, A dark matter relic from muon anomalies, Phys. Rev. D **92**, 055021 (2015).

[38] A. Celis, W.-Z. Feng, and M. Vollmann, Dirac dark matter and $b \to s\ell^+\ell^-$ with U(1) gauge symmetry, Phys. Rev. D **95,** 035018 (2017).

[39] W. Altmannshofer, S. Gori, S. Profumo, and F. S. Queiroz, Explaining dark matter and B decay anomalies with an $L_\mu - L_\tau$ model, J. High Energy Phys. 12 (2016) 106.

[40] P. Ko, T. Nomura, and H. Okada, A flavor dependent gauge symmetry, predictive radiative seesaw and LHCb anomalies, Phys. Lett. B **772,** 547 (2017).

[41] P. Ko, T. Nomura, and H. Okada, Explaining $B \to K^{(*)}\ell^+\ell^-$ anomaly by radiatively induced coupling in $U(1)_{\mu-\tau}$ gauge symmetry, Phys. Rev. D **95,** 111701 (2017).

[42] J. M. Cline, J. M. Cornell, D. London, and R. Watanabe, Hidden sector explanation of B-decay and cosmic ray anomalies, Phys. Rev. D **95,** 095015 (2017).

[43] S. Baek, Dark matter contribution to $b \to s\mu^+\mu^-$ anomaly in local $U(1)_{L_\mu - L_\tau}$ model, Phys. Lett. B **781,** 376 (2018).

[44] J. M. Cline, B decay anomalies and dark matter from vectorlike confinement, Phys. Rev. D **97,** 015013 (2018).

[45] A. Falkowski, S. F. King, E. Perdomo, and M. Pierre, Flavourful Z' portal for vector-like neutrino dark matter and $R_{K^{(*)}}$, J. High Energy Phys. 08 (2018) 061.

[46] G. Arcadi, T. Hugle, and F. S. Queiroz, The dark $L_\mu - L_\tau$ rises via kinetic mixing, Phys. Lett. B **784,** 151 (2018).

[47] S. Baek and C. Yu, Dark matter for $b \to s\mu^+\mu^-$ anomaly in a gauged $U(1)_X$ model, J. High Energy Phys. 11 (2018) 054.

[48] A. Vicente, Flavor and dark matter connection, Springer Proc. Phys. **234,** 393 (2019).

[49] S. Baek, Scalar dark matter behind $b \to s\mu\mu$ anomaly, J. High Energy Phys. 05 (2019) 104.

[50] L. Calibbi, T. Li, Y. Li, and B. Zhu, Simple model for large CP violation in charm decays, B-physics anomalies, muon $g - 2$ and dark matter, J. High Energy Phys. 10 (2020) 070.

[51] S.-P. Li and X.-Q. Li, Probing new physics signals with symmetry-restored Yukawa textures, Eur. Phys. J. C **80,** 268 (2020).

[52] L. Darmé, M. Fedele, K. Kowalska, and E. M. Sessolo, Flavour anomalies from a split dark sector, J. High Energy Phys. 08 (2020) 148.

[53] A. Kachanovich, U. Nierste, and I. Nišandžić, Higgs portal to dark matter and $B \to K^{(*)}$ decays, Eur. Phys. J. C **80,** 669 (2020).

[54] D. Guadagnoli, M. Reboud, and P. Stangl, The dark side of 4321, J. High Energy Phys. 10 (2020) 084.

[55] D. Borah, L. Mukherjee, and S. Nandi, Low scale $U(1)_X$ gauge symmetry as an origin of dark matter, neutrino mass and flavour anomalies, J. High Energy Phys. 12 (2020) 052.

[56] A. Carvunis, D. Guadagnoli, M. Reboud, and P. Stangl, Composite dark matter and a horizontal symmetry, J. High Energy Phys. 02 (2021) 056.

[57] F. D'Eramo, N. Košnik, F. Pobbe, A. Smolkovič, and O. Sumensari, Leptoquarks and real singlets: A richer scalar sector behind the origin of dark matter, Phys. Rev. D **104,** 015035 (2021).

[58] W. Chao, H. Wang, L. Wang, and Y. Zhang, Dark matter, Z', vector-like quark at the LHC and $b \to s\mu\mu$ anomaly, Chin. Phys. C **45,** 083105 (2021).

[59] M. Cirelli, N. Fornengo, and A. Strumia, Minimal dark matter, Nucl. Phys. **B753,** 178 (2006).

[60] J. Hisano, K. Ishiwata, N. Nagata, and T. Takesako, Direct detection of electroweak-interacting dark matter, J. High Energy Phys. 07 (2011) 005.

[61] R. Aaij *et al.* (LHCb Collaboration), Measurement of the $B_s^0 \to \mu^+\mu^-$ Branching Fraction and Effective Lifetime and Search for $B^0 \to \mu^+\mu^-$ Decays, Phys. Rev. Lett. **118,** 191801 (2017).

[62] S. Chatrchyan *et al.* (CMS Collaboration), Measurement of the $B_s^0 \to \mu^+\mu^-$ Branching Fraction and Search for $B^0 \to \mu^+\mu^-$ with the CMS Experiment, Phys. Rev. Lett. **111,** 101804 (2013).

[63] M. Aaboud *et al.* (ATLAS Collaboration), Study of the rare decays of B_s^0 and B^0 mesons into muon pairs using data collected during 2015 and 2016 with the ATLAS detector, J. High Energy Phys. 04 (2019) 098.

[64] Y. Amhis *et al.* (HFLAV Collaboration), Averages of b-hadron, c-hadron, and τ-lepton properties as of summer 2016, Eur. Phys. J. C **77,** 895 (2017).

[65] R. Aaij *et al.* (LHCb Collaboration), Measurement of the ratio of branching fractions $\mathrm{BR}(B_0 \to K^{\star 0}\gamma)/\mathrm{BR}(B_{s0} \to \phi\gamma)$ and the direct CP asymmetry in $B_0 \to K^{\star 0}\gamma$, Nucl. Phys. **B867,** 1 (2013).

[66] L. Di Luzio, M. Kirk, A. Lenz, and T. Rauh, ΔM_s theory precision confronts flavour anomalies, J. High Energy Phys. 12 (2019) 009.

[67] L. Di Luzio, M. Kirk, and A. Lenz, Updated B_s-mixing constraints on new physics models for $b \to s\ell^+\ell^-$ anomalies, Phys. Rev. D **97,** 095035 (2018).

[68] J. De Blas *et al.*, HEPfit: A code for the combination of indirect and direct constraints on high energy physics models, Eur. Phys. J. C **80,** 456 (2020).

[69] T. Aoyama *et al.*, The anomalous magnetic moment of the muon in the standard model, Phys. Rep. **887,** 1 (2020).

[70] L. Calibbi, R. Ziegler, and J. Zupan, Minimal models for dark matter and the muon $g - 2$ anomaly, J. High Energy Phys. 07 (2018) 046.

[71] K. Kowalska and E. M. Sessolo, Expectations for the muon $g - 2$ in simplified models with dark matter, J. High Energy Phys. 09 (2017) 112.

[72] A. M. Sirunyan *et al.* (CMS Collaboration), Search for supersymmetry in proton-proton collisions at 13 TeV in final states with jets and missing transverse momentum, J. High Energy Phys. 10 (2019) 244.

[73] G. Aad *et al.* (ATLAS Collaboration), Search for electroweak production of charginos and sleptons decaying into final states with two leptons and missing transverse momentum in $\sqrt{s} = 13$ TeV pp collisions using the ATLAS detector, Eur. Phys. J. C **80,** 123 (2020).

[74] G. Aad *et al.* (ATLAS Collaboration), Searches for electroweak production of supersymmetric particles with compressed mass spectra in $\sqrt{s} = 13$ TeV pp collisions with the ATLAS detector, Phys. Rev. D **101,** 052005 (2020).

[75] A. M. Sirunyan *et al.* (CMS Collaboration), Search for new physics in events with two soft oppositely charged leptons and missing transverse momentum in proton-proton collisions at $\sqrt{s} = 13$ TeV, Phys. Lett. B **782,** 440 (2018).

[76] A. M. Sirunyan *et al.* (CMS Collaboration), Search for top squark pair production using dilepton final states in pp collision data collected at $\sqrt{s} = 13$ TeV, Eur. Phys. J. C **81**, 3 (2021).

[77] ATLAS Collaboration, Search for new phenomena in events with two opposite-charge leptons, jets and missing transverse momentum in pp collisions at $\sqrt{s} = 13$ TeV with the ATLAS detector, Report No. ATLAS-CONF-2020-046.

[78] Y. Yamada, Electroweak two-loop contribution to the mass splitting within a new heavy $SU(2)_L$ fermion multiplet, Phys. Lett. B **682**, 435 (2010).

[79] M. Ibe, S. Matsumoto, and R. Sato, Mass splitting between charged and neutral winos at two-loop level, Phys. Lett. B **721**, 252 (2013).

[80] M. Aaboud *et al.* (ATLAS Collaboration), Search for long-lived charginos based on a disappearing-track signature in pp collisions at $\sqrt{s} = 13$ TeV with the ATLAS detector, J. High Energy Phys. 06 (2018) 022.

[81] A. M. Sirunyan *et al.* (CMS Collaboration), Search for disappearing tracks in proton-proton collisions at $\sqrt{s} = 13$ TeV, Phys. Lett. B **806**, 135502 (2020).

[82] A. Alloul, N. D. Christensen, C. Degrande, C. Duhr, and B. Fuks, FeynRules 2.0—A complete toolbox for tree-level phenomenology, Comput. Phys. Commun. **185**, 2250 (2014).

[83] J. Alwall, R. Frederix, S. Frixione, V. Hirschi, F. Maltoni, O. Mattelaer, H. S. Shao, T. Stelzer, P. Torrielli, and M. Zaro, The automated computation of tree-level and next-to-leading order differential cross sections, and their matching to parton shower simulations, J. High Energy Phys. 07 (2014) 079.

[84] T. Sjöstrand, S. Ask, J. R. Christiansen, R. Corke, N. Desai, P. Ilten, S. Mrenna, S. Prestel, C. O. Rasmussen, and P. Z. Skands, An introduction to PYTHIA 8.2., Comput. Phys. Commun. **191**, 159 (2015).

[85] J. de Favereau, C. Delaere, P. Demin, A. Giammanco, V. Lemaître, A. Mertens, and M. Selvaggi (DELPHES 3 Collaboration), DELPHES 3, A modular framework for fast simulation of a generic collider experiment, J. High Energy Phys. 02 (2014) 057.

[86] D. Dercks, N. Desai, J. S. Kim, K. Rolbiecki, J. Tattersall, and T. Weber, CheckMATE 2: From the model to the limit, Comput. Phys. Commun. **221**, 383 (2017).

[87] J. S. Kim, D. Schmeier, J. Tattersall, and K. Rolbiecki, A framework to create customised LHC analyses within CheckMATE, Comput. Phys. Commun. **196**, 535 (2015).

[88] Y. Bai and J. Berger, Fermion portal dark matter, J. High Energy Phys. 11 (2013) 171.

[89] Y. Bai and J. Berger, Lepton portal dark matter, J. High Energy Phys. 08 (2014) 153.

[90] G. Arcadi, M. Dutra, P. Ghosh, M. Lindner, Y. Mambrini, M. Pierre, S. Profumo, and F. S. Queiroz, The waning of the WIMP? A review of models, searches, and constraints, Eur. Phys. J. C **78**, 203 (2018).

[91] K. A. Mohan, D. Sengupta, T. M. P. Tait, B. Yan, and C. P. Yuan, Direct detection and LHC constraints on a *t*-channel simplified model of majorana dark matter at one loop, J. High Energy Phys. 05 (2019) 115.

[92] C. Arina, B. Fuks, and L. Mantani, A universal framework for t-channel dark matter models, Eur. Phys. J. C **80**, 409 (2020).

[93] C. Arina, B. Fuks, L. Mantani, H. Mies, L. Panizzi, and J. Salko, Closing in on *t*-channel simplified dark matter models, Phys. Lett. B **813**, 136038 (2021).

[94] J. Kawamura, S. Okawa, and Y. Omura, Current status and muon $g - 2$ explanation of lepton portal dark matter, J. High Energy Phys. 08 (2020) 042.

[95] S. Okawa and Y. Omura, Light mass window of lepton portal dark matter, J. High Energy Phys. 02 (2021) 231.

[96] P. Agrawal, S. Blanchet, Z. Chacko, and C. Kilic, Flavored dark matter, and its implications for direct detection and colliders, Phys. Rev. D **86**, 055002 (2012).

[97] P. Agrawal, M. Blanke, and K. Gemmler, Flavored dark matter beyond Minimal Flavor Violation, J. High Energy Phys. 10 (2014) 072.

[98] M. Blanke and S. Kast, Top-flavoured dark matter in dark minimal flavour violation, J. High Energy Phys. 05 (2017) 162.

[99] M. Blanke, P. Pani, G. Polesello, and G. Rovelli, Single-top final states as a probe of top-flavoured dark matter models at the LHC, J. High Energy Phys. 01 (2021) 194.

[100] Y. Liu, B. Yan, and R. Zhang, Loop induced top quark FCNC through top quark and dark matter interactions, arXiv:2103.07859.

[101] N. Aghanim *et al.* (Planck Collaboration), Planck 2018 results. VI. Cosmological parameters, Astron. Astrophys. **641**, A6 (2020).

[102] P. Gondolo and G. Gelmini, Cosmic abundances of stable particles: Improved analysis, Nucl. Phys. **B360**, 145 (1991).

[103] J. Edsjo and P. Gondolo, Neutralino relic density including coannihilations, Phys. Rev. D **56**, 1879 (1997).

[104] S. Biondini and S. Vogl, Coloured coannihilations: Dark matter phenomenology meets non-relativistic EFTs, J. High Energy Phys. 02 (2019) 016.

[105] S. Biondini and S. Vogl, Scalar dark matter coannihilating with a coloured fermion, J. High Energy Phys. 11 (2019) 147.

[106] F. Giacchino, A. Ibarra, L. Lopez Honorez, M. H. G. Tytgat, and S. Wild, Signatures from scalar dark matter with a vector-like quark mediator, J. Cosmol. Astropart. Phys. 02 (2016) 002.

[107] R. Iengo, Sommerfeld enhancement: General results from field theory diagrams, J. High Energy Phys. 05 (2009) 024.

[108] J. L. Feng, M. Kaplinghat, and H.-B. Yu, Sommerfeld enhancements for thermal relic dark matter, Phys. Rev. D **82**, 083525 (2010).

[109] A. Hryczuk and R. Iengo, The one-loop and Sommerfeld electroweak corrections to the Wino dark matter annihilation, J. High Energy Phys. 01 (2012) 163.

[110] M. Beneke, C. Hellmann, and P. Ruiz-Femenia, Heavy neutralino relic abundance with Sommerfeld enhancements—a study of pMSSM scenarios, J. High Energy Phys. 03 (2015) 162.

[111] A. Mitridate, M. Redi, J. Smirnov, and A. Strumia, Cosmological implications of dark matter bound states, J. Cosmol. Astropart. Phys. 05 (2017) 006.

[112] G. Arcadi and P. Ullio, Accurate estimate of the relic density and the kinetic decoupling in non-thermal dark matter models, Phys. Rev. D **84,** 043520 (2011).

[113] M. Drees and F. Hajkarim, Dark matter production in an early matter dominated era, J. Cosmol. Astropart. Phys. 02 (2018) 057.

[114] E. Aprile *et al.* (XENON Collaboration), Dark Matter Search Results from a One Ton-Year Exposure of XENON1T, Phys. Rev. Lett. **121,** 111302 (2018).

[115] J. Hisano, R. Nagai, and N. Nagata, Effective theories for dark matter nucleon scattering, J. High Energy Phys. 05 (2015) 037.

[116] B. Bhattacharya, D. London, J. M. Cline, A. Datta, and G. Dupuis, Quark-flavored scalar dark matter, Phys. Rev. D **92,** 115012 (2015).

[117] J. L. Feng, J. Kumar, and D. Sanford, Xenophobic dark matter, Phys. Rev. D **88,** 015021 (2013).

[118] A. Ibarra and S. Wild, Dirac dark matter with a charged mediator: A comprehensive one-loop analysis of the direct detection phenomenology, J. Cosmol. Astropart. Phys. 05 (2015) 047.

[119] J. D. Lewin and P. F. Smith, Review of mathematics, numerical factors, and corrections for dark matter experiments based on elastic nuclear recoil, Astropart. Phys. **6,** 87 (1996).

[120] T. Banks, J.-F. Fortin, and S. Thomas, Direct detection of dark matter electromagnetic dipole moments, arXiv:1007.5515.

[121] J. Hisano, R. Nagai, and N. Nagata, Singlet dirac fermion dark matter with mediators at loop, J. High Energy Phys. 12 (2018) 059.

[122] J. Hisano, K. Ishiwata, and N. Nagata, A complete calculation for direct detection of Wino dark matter, Phys. Lett. B **690,** 311 (2010).

[123] M. Ahnen *et al.* (MAGIC, Fermi-LAT Collaborations), Limits to dark matter annihilation cross-section from a combined analysis of MAGIC and Fermi-LAT observations of dwarf satellite galaxies, J. Cosmol. Astropart. Phys. 02 (2016) 039.

[124] S. Hoof, A. Geringer-Sameth, and R. Trotta, A global analysis of dark matter signals from 27 dwarf spheroidal galaxies using 11 years of Fermi-LAT Observations, J. Cosmol. Astropart. Phys. 02 (2020) 012.

[125] R. Barbieri, L. J. Hall, and V. S. Rychkov, Improved naturalness with a heavy Higgs: An alternative road to LHC physics, Phys. Rev. D **74,** 015007 (2006).

[126] L. Lopez Honorez, E. Nezri, J. F. Oliver, and M. H. G. Tytgat, The inert doublet model: An archetype for dark matter, J. Cosmol. Astropart. Phys. 02 (2007) 028.

[127] L. Lopez Honorez and C. E. Yaguna, The inert doublet model of dark matter revisited, J. High Energy Phys. 09 (2010) 046.

[128] L. Lopez Honorez and C. E. Yaguna, A new viable region of the inert doublet model, J. Cosmol. Astropart. Phys. 01 (2011) 002.

[129] G. Gelmini, P. Gondolo, A. Soldatenko, and C. E. Yaguna, The effect of a late decaying scalar on the neutralino relic density, Phys. Rev. D **74,** 083514 (2006).

[130] G. B. Gelmini and P. Gondolo, Neutralino with the right cold dark matter abundance in (almost) any supersymmetric model, Phys. Rev. D **74,** 023510 (2006).

[131] P. Arias, N. Bernal, A. Herrera, and C. Maldonado, Reconstructing non-standard cosmologies with dark matter, J. Cosmol. Astropart. Phys. 10 (2019) 047.

[132] M. Cirelli, F. Sala, and M. Taoso, Wino-like Minimal Dark Matter and future colliders, J. High Energy Phys. 10 (2014) 033.

[133] J. Hisano, K. Ishiwata, and N. Nagata, QCD effects on direct detection of wino dark matter, J. High Energy Phys. 06 (2015) 097.

[134] C.-W. Chiang, G. Cottin, Y. Du, K. Fuyuto, and M. J. Ramsey-Musolf, Collider probes of real triplet scalar dark matter, J. High Energy Phys. 01 (2021) 198.

[135] J. Arakawa and T. M. P. Tait, Is a miracle-less WIMP ruled out?, SciPost Phys. **11,** 019 (2021).

[136] E. Aprile *et al.* (XENON Collaboration), Projected WIMP sensitivity of the XENONnT dark matter experiment, J. Cosmol. Astropart. Phys. 11 (2020) 031.

[137] L. Di Luzio, R. Gröber, and G. Panico, Probing new electroweak states via precision measurements at the LHC and future colliders, J. High Energy Phys. 01 (2019) 011.

[138] A. Crivellin, M. Hoferichter, and P. Schmidt-Wellenburg, Combined explanations of $(g-2)_{\mu,e}$ and implications for a large muon EDM, Phys. Rev. D **98,** 113002 (2018).

[139] G. Arcadi, L. Calibbi, M. Fedele, and F. Mescia, Muon $g-2$ and B Anomalies from Dark Matter, Phys. Rev. Lett. **127,** 061802 (2021).